Elevated temperature fatally disrupts nuclear divisions in the early *Drosophila* embryo.

Girish Kale[1,*], Pratika Agarwal[1], J Jaime Diaz-Larrosa[1], Steffen Lemke[1,2,*]

[1] Centre for Organismal Studies, University of Heidelberg, Heidelberg. Germany
[2] Institute of Biology, University of Hohenheim, Stuttgart, Germany
* Correspondance: G.K. (girish.kale@cos.uni-heidelberg.de), S.L. (steffen.lemke@uni-hohenheim.de)

Abstract:

Temperature fluctuations can challenge animal survival, especially in embryos of animals that can't actively regulate their body temperature. Previous work in insects suggests that spatial gradients and temporal variations in temperature can affect embryonic development in a region-specific manner. Yet, it is unclear if elevated temperature produces developmental defects, and if so, how the disruption may manifest. Here we use early embryonic development of the fruit fly *Drosophila melanogaster* as a model to address consequences of elevated temperature on fly embryonic development.

We identified the syncytial blastoderm stage as a critical time window as being particularly sensitive to elevated temperature. During the syncytial blastoderm stage involves 4 rounds of meta-synchronous nuclear divisions at the embryo cortex, followed by cellularization to form the cellular blastoderm. Live imaging these processes at elevated temperature revealed an increase in mitotic failures and a loss of cortical nuclei, both, during syncytial- and cellular-blastoderm stage. Additionally, embryos developing at elevated temperature show a local crowding of nuclei and an increase in asynchrony between the nuclear cycles in the middle vs anterior/posterior poles. Interestingly, nuclear crowding and nuclear cycle asynchrony cooperatively amplify the frequency of mitotic failures, leading to holes in the blastoderm epithelium. Strikingly, the exposure to elevated temperature during this developmental stage also increased embryonic lethality. We propose that the loss of nuclei results in a loss of patterning information and the abrogation of proper embryonic development. We identified genes that regulate mitosis, especially the ones mediating the interaction between microtubules and F-actin, and functionally tested their capacity to rescue the embryonic lethality.

Our results expose a vulnerability at elevated temperatures in the interaction between cortical actin and microtubules, which leads to mitotic failures, and can be potentially rescued by modulating the expression of just a few factors. We propose that the expression levels of the corresponding genes could be used as indicators to predict fitness effects on insect populations that are exposed to increasing temperature variations.

Introduction:

Temperature is a key factor determining the fidelity of embryonic development. Studies have shown occurrence of birth defects due to hyperthermia during pregnancy (Edwards 2006; Miller and Church 2013; Graham 2020), in spite of active regulation of core temperature. Here, the cell biological basis for the developmental defects due to an exposure to high temperature, remains elusive. It is currently unclear whether this phenomenon could be observed and studied also in invertebrate species, for which the developmental process is well described, allowing for a quantitative characterization of the potential developmental defects arising due to high temperature. Here we explore whether the exposure to high temperature is detrimental to the development in the embryos of *Drosophila melanogaster* (henceforth, *Drosophila*), addressing the cell biological basis for possible defects, and asking what are the consequences in terms of population level parameters, such as embryo survival.

Previous studies have shown that the early embryonic development of *Drosophila* embryos (first ~6 hours) is especially sensitive to acute heat shock (Welte et al. 1993), and have indicated that acute heat shock causes a loss of coordination in developmental processes to induce developmental defects (Crews, McCleery, and Hutson 2016). Given that the survival after a heat shock relies on transcription of heat-shock proteins (Graziosi et al. 1980), and that zygotic transcription is progressively activated during maternal-to-zygotic transition (Pritchard and Schubiger 1996), it is likely that the developmental processes prior to the completion of this transition are especially susceptible to heat shock. In line with these expectations, previous studies have demonstrated a disruption of the normal dynamics of cytoskeletal elements due to an exposure to high temperature (Walter, Petersen, and Biessmann 1990; Zheng et al. 2013; Figard et al. 2019). Even more elusive are the effects of prolonged exposure to elevated temperature below the heat shock limits. Here we focus on such temperature sensitivity of early embryonic development in *Drosophila*, and ask what is the cell biological basis for developmental defects due to an exposure to elevated temperature, and whether there is a link to the population level consequences on embryo survival.

Post fertilization, the *Drosophila* embryos undergo 9 rounds of syncytial nuclear divisions deep in the yolk. Following these divisions, most nuclei migrate to embryo periphery, where 4 more rounds of nuclear division take place during a stage called, syncytial blastoderm (Foe and Alberts 1983). These nuclear divisions are facilitated by pseudo-cleavage furrows, i.e., temporary membrane invaginations resembling a half-cell that slowly form around the nuclei during interphase-metaphase, and are then rapidly reabsorbed into the embryo cortex during anaphase-telophase (Xie and Blankenship 2018). Following these 13 rounds of nuclear divisions, the resulting ~6000 nuclei simultaneously segregate into individual cells, in the process of cellularization, producing the blastoderm epithelium (Mazumdar and Mazumdar 2002). At this point gastrulation starts, which involves cell shape changes (Martin 2020), cell contact rearrangements (Lecuit and Yap 2015), and further rounds of cell divisions in isolated mitotic domains (Foe 1989): all facilitating the early morphogenesis. Cell biological basis for these early developmental processes is well described, and would allow us to identify the defects at elevated temperature, if any.

In our experiments, we exposed *Drosophila* embryos to the elevated temperature, and compared them with normal temperature controls. Following previous studies, we chose 29°C as elevated temperature (Kuntz and Eisen 2014; Chong, Amourda, and Saunders 2018) and asked whether increased temperature up to 29°C resulted in developmental defects. Notably, this temperature is well below the 32°C and higher range required to elicit a robust heat shock response (Vazquez, Pauli,

and Tissières 1993), and no major developmental defects have been reported so far at 29°C. We found that exposing embryos to elevated temperature during early embryonic development leads to a significant increase in the population level embryonic lethality. When we traced defects from the organism to the cellular level, we observed a loss of nuclei during syncytial- and cellular-blastoderm stage, which was caused by mitotic failures. Additionally, in embryos developing at elevated temperature, we observed and quantified the nuclear crowding in the central region of the embryo, as well as greater asynchrony in the nuclear division cycles between central regions vs anterior/posterior poles of the embryo. What's more, we could show that the nuclear crowding and nuclear cycle asynchrony combinatorially cooperate to locally increase the propensity of mitotic failures. Such local increase in mitotic failures results in holes in the blastoderm, i.e., region devoid of nuclei/cells, to disrupt the continuity of this primary epithelial tissue. We overexpressed a few candidate genes to boost the robustness of nuclear divisions to rescue the mitotic failures defect, focusing on the regulators of cell polarity, microtubule- F-actin interactions, and mitotic spindle orientation, to test their ability to rescue the described defects, and ameliorate the embryo lethality at elevated temperature. Our results suggest a vulnerability in microtubule- F-actin interaction during the well conserved process of nuclear division, when occurring at elevated temperature. Our work establishes a novel link between cell biological defects due to an exposure to elevated temperature, and a reduction in organismal fitness at population level at elevated temperature.

Results:

Early exposure to elevated temperature reduces embryo survival.

To test whether elevated temperature had an effect on developmental robustness during the first hours of embryonic development, we exposed young embryos to 29°C and asked whether this would alter the fraction of embryos that hatch into larvae. To associate possible fitness effects with defined developmental windows (see above), embryos were exposed to elevated temperature either from deposition till before the onset of gastrulation (~3 hours) or for a duration of ~3 hours from the onset of gastrulation (Figure 1A), to keep the temperature exposures comparable. In both cases we observed a significant increase in embryonic lethality (Figure 1B). Our findings reveal a particular vulnerability during the syncytial phase of embryonic fly development and suggest that elevated temperature leads to defects in the setup of the insect blastoderm. This is surprising because previous studies indicated that genetic patterning and setting up of positional information within the blastoderm was overall robust against temperature fluctuations (Lucchetta et al. 2005; Niemuth and Wolf 1995).

In addition to genetic patterning, nuclear dynamics could be challenged during the first hours of embryonic development. In this developmental window, nuclei divide deep in the yolk, then translocate to the embryo cortex, where they need to be anchored robustly while undergoing further rounds of nuclear division. A normal distribution of nuclei ultimately determines a normal morphogenesis of the blastoderm epithelium. Thus, to address whether defects in the blastoderm could stem from defects in nuclear dynamics, we analyzed behavior of syncytial nuclei as they translocated to the egg cortex and divided. To follow nuclear dynamics during blastoderm formation, we used Histone-RFP to visualize nuclei, and Jupiter-GFP to visualize microtubules, keeping track of nuclear division cycles. Starting with nuclear migration from the yolk to periphery (occurring during the interphase of the 10th nuclear cycle), we observed nuclei through their peripheral divisions during syncytial blastoderm (mitoses 10 through 13), and then through cellularization (interphase 14), until the onset of gastrulation could be inferred from the movement

123 and division of nuclei (beyond interphase 14). During this time window, in embryos developing at
124 elevated temperature, we did not observe any significant defects in nuclear distribution, as they
125 translocated normally from deep inside the yolk to embryo cortex. However, embryos that
126 developed at 29°C much more frequently "lost" nuclei from their cortical layer than if they
127 developed at 25°C, i.e., nuclei that were initially positioned within the cortical layer of the egg,
128 appeared to get expelled, descended into the yolk, and did not become part of the embryonic
129 blastoderm (Figure 1C-E), with a variability in the extent of the nuclear loss, producing holes in the
130 blastoderm of a fraction of embryos (Figure S1). Further, in the embryos fixed and stained with
131 DRAQ5, we imaged the nuclear distribution in the entire embryo volume, to observe that the loss of
132 nuclei wasn't symmetric in the two halves of the embryos, and albeit in the central region of the
133 embryos, the location of the nuclear loss varied across embryos (Figure S2). The embryo-to-embryo
134 variability, both in the distribution and intensity of nuclear loss argued for the possibility that these
135 defects were self-organized rather than dictated by the genetic make-up.

136 Taken together, we identified the syncytial blastoderm stage of embryo development as the most
137 sensitive window, based on the embryo lethality analysis. Additionally, the loss of nuclei during this
138 stage indicated a defect in nuclear anchorage at the embryo cortex, rather than nuclear divisions
139 deep in the yolk, or the translocation of nuclei from deep inside the yolk to the embryo cortex.

140 A closer observation of live imaged embryos revealed three striking phenomena during blastoderm
141 formation in embryos developing at elevated temperature compared to normal temperature
142 controls: an extensive loss of nuclei from the egg cortex (as above), a time shift and slowdown of
143 nuclear divisions cycles in the central region of the embryo compared to its poles, and nuclear
144 crowding in the central region of the embryo. Thus, we decided to quantitatively describe these
145 defects, in an attempt to describe the necessary conditions to produce a blastoderm hole, and link
146 these defects to the embryo lethality phenotype.

147 **At elevated temperature, embryos lose nuclei from the cortex after defective divisions.**
148 A closer look at the loss of cortical nuclei indicated that the nuclei were lost either individually or as
149 pairs of two adjacent nuclei. We could also observe periods of drastic displacement of nuclei at
150 elevated temperature (see below). Based on these observations, we imagined various mechanisms
151 for the observed loss of nuclei. For instance, individual nuclei might be lost due to out-of-plane
152 nuclear divisions, while a pair of nuclei might be lost due to a defective in-plane nuclear division. In
153 case of defects in nuclear divisions, it is possible that the cell cycle checkpoints are triggered. Nuclei
154 being dislodged from the embryo cortex during the drastic displacements could also explain both
155 individual and pairwise loss, though in such scenario, whether the pairs of nuclei need to be
156 somehow associated with each other, influencing each other's loss. Here we considered these
157 possibilities, and asked to what extent do they account for the observed loss of nuclei.

158 To address whether cortical nuclei appeared as getting lost because of an increased frequency of
159 out-of-plane divisions, we visually tracked nuclei from their last division to the time they were no
160 longer associated with the cortex. We could detect out-of-plane divisions in embryos at
161 temperatures ranging from 22 to 29°C, only during the mitoses of the 10th nuclear cycle. These out-
162 of-plane divisions could be easily identified, as they formed a characteristic mitotic spindle that was
163 oriented perpendicular to the embryo surface (Figure S3A, B), and after the division only one of the
164 daughter nuclei remained attached to the cortex. However, the overall frequency of out-of-plane
165 divisions was very low (<5%): neither did it differ significantly between any of the observed

166 temperatures (Figure S3C), nor could it explain the loss of nuclei during later nuclear cycles.
167 Similarly, losses of individual nuclei after an in-plane division were rather infrequent, and did not
168 differ significantly within the range of observed temperatures (Figure S3D, E). This suggested that
169 the increased loss of nuclei observed in embryos developing at 29°C could neither be accounted for
170 with individual nuclei dropping into the yolk, irrespective of whether the loss was due to them being
171 mechanically dislodged.

172 For the observed pairwise loss of nuclei, our tracking revealed that these were sister nuclei born
173 from the same mitosis. This suggested that specific characteristics of cortical nuclear divisions might
174 determine the future fate of the newborn nuclei and trigger their release from the egg cortex,
175 possibly in response to failed checkpoints during mitosis. In all of the pairwise loss of nuclei, we
176 observed chromosome segregation defects (Figure 1F) that could lead to aneuploidy, suggesting that
177 the subsequent expulsion of daughter nuclei from the egg cortex was caused by a defective mitosis.
178 Following defective mitoses either at normal or elevated temperature, we could not detect a clear
179 time course of nuclear expulsion as the corresponding nuclei could be lost in the immediately
180 following or in later interphases (Figure S4), suggesting that nuclear expulsion after defective mitosis
181 was a passive process and not triggered by molecular signaling at failed checkpoints.

182 To confirm that the observed loss of nuclei at 29°C could be attributed to an overall increase in
183 defective mitoses, we asked if the frequency of defective mitoses was changing depending on the
184 temperature. To address this question, we focused on interphase 14, as that's when we observed
185 the most nuclear losses, and counted the pairwise loss of nuclei after mitotic failures at 22, 25, 28,
186 and 29°C (see methods). While the frequency of mitotic failures was overall low at 22 to 28°C, it
187 increased significantly at 29°C (Figure 1G). Taken together, our findings identify nuclear divisions in
188 the blastoderm as a thermolabile cellular process (Figure 1H) that shows a disproportionate increase
189 in failures at the transition from 28°C to 29°C, resulting in the loss of defectively born sister nuclei
190 from the egg cortex. Interestingly, in a fraction of embryos the mitotic failures occurred in great
191 numbers and in close vicinity, leading to the holes in the blastoderm epithelium (Figure 1G, hollow
192 markers). Thus, the formation of blastoderm holes (Figure S1) could be directly attributed to
193 clustered mitotic failures, though it remained unclear why some embryos have the aggregates of
194 mitotic failures while others didn't.

195 To explore the potential cause of mitotic failures at elevated temperatures, we tracked nuclear
196 clusters starting from individual mother nucleus (end of interphase 10) to the 8 great-granddaughter
197 nuclei (end of interphase 13), in order to quantitatively describe their movement (Figure S5A-C). This
198 allowed us to assess mechanical stresses that would be experienced by nuclei dividing at the
199 blastoderm cortex, as we distinguished the movement of nuclear clusters during interphase-
200 metaphase vs. anaphase-telophase. Our results showed that the nuclear clusters had 2 components
201 to their movement. First, the clusters exhibited a constant drift-like movement, which we captured
202 using a linear fit to the displacement of the center of the nuclear clusters over time (Figure S5B
203 dotted lines). The slope of the linear fit indicated that the clusters drifted towards posterior (Figure
204 S5D, E). The second component was composed of deviations in the centers of nuclear cluster from
205 the linear fit, i.e., the displacements relative to the first component. These deviations were
206 significantly greater at elevated temperature, both during the interphase-metaphase period (Figure
207 S5F, G) and during the anaphase-telophase period (Figure S5H, I), though the displacements along
208 AP-axis were more drastic than those along DV-axis, and those during anaphase-telophase were 2-3-
209 fold greater than those during interphase-metaphase. For context, the length scale of the

210 displacements during anaphase-telophase could be up to 4-times the length of the spindle itself,
211 indicating an extensive propensity for displacement in x-y plane, especially along the AP axis. We
212 also observed that the spindles were getting displaced in z-axis, again, during anaphase-telophase
213 period. In embryos developing at 29°C, we could see two waves of nuclear displacement, originating
214 from the anterior and the posterior pole, meeting at the central region of the embryo (Figure S6).
215 Overall, these quantifications and observations indicated that the mitotic spindles are displaced
216 drastically while nuclei are dividing, and argued for the possibility of mechanical defects during
217 nuclear divisions.

218 Taken together, we observed the effects of exposure to elevated temperature, at organismal level as
219 embryo lethality (Figure 1B), at tissue level as blastoderm holes (Figure 1E, Figure S1, S2), and at
220 cellular level as mitotic failures (Figure 1F, G). Embryos with most severe form of mitotic failure
221 phenotype had blastoderm hole, while the fraction of embryos with large blastoderm holes
222 correlated well with increase in embryo lethality, indicting a link from cellular till organismal
223 phenotype. Given that the loss of nuclei occurs after mitosis, and that the nuclei move drastically
224 during anaphase-telophase period, we further argue that nuclear anchorage is specifically
225 challenged during mitosis.

226 **Nuclei divide with a time shift and are crowded in embryos at elevated temperature.**
227 The most severe loss of nuclei was often observed in the central domain of the embryo (Figure 1C-E,
228 Figure S1 and S2). Notably, these areas coincided with the "collision" of two waves of nuclear
229 displacements along z-axis (Figure S6), i.e., the future apical-basal axis in the blastoderm cells (A.
230 Schmidt and Grosshans 2018). We could further observe that, not only anaphase, but all other
231 phases of nuclear division were delayed in the central region of the embryos developing at 29°C. This
232 resulted in regions of embryo being segregated into domains of nuclear division phases (Figure 2A).
233 Conversely, the same phase of nuclear division cycle could be observed at different timepoints in
234 different regions of the embryo (Figure S7). Thus, we decided to quantify this asynchrony of nuclear
235 division cycles as a function of temperature (see methods, also Figure S7). Our quantifications show
236 that the asynchrony significantly increases in embryos developing at 29°C as compared to other
237 temperatures (Figure 2B). Thus, we quantitatively describe the defect of asynchrony in nuclear
238 cycles at elevated temperature (Figure 2C).

239 To quantify nuclear crowding, we focused on the last nuclear division cycle and its preceding
240 interphase (interphase 13, see methods). To quantify the space available for cortical blastoderm
241 nuclei, we used Voronoi tessellation and measured distances between nuclei using pseudo-cell area.
242 The distances between nuclei overall were rather homogeneous in embryos developing at 22°C
243 (Figure 2D, H, L). Already at 25°C (Figure 2E, I, M) and 28°C (Figure 2F, J, n), the available space for
244 cortical nuclei was no longer uniform across the embryo, and it showed signs of local crowding. At
245 29°C, the space available for nuclei along the anterior-posterior axis varied substantially and
246 revealed strong nuclear crowding in the central region of the embryo (Figure 2G, K, O). We
247 quantified the extent of crowding (see methods) as a function of temperature, and found a
248 progressive increase in the nuclear crowding (Figure 2P). Thus, we also quantitatively describe the
249 defect of nuclear crowding at elevated temperature (Figure 2Q).

250 Taken together, we have two additional defects at elevated temperature, nuclear crowding and
251 nuclear cycle asynchrony, besides mitotic failures. We also note that the severity of these defects
252 (based on the quantifications) can vary between embryos, e.g., the embryos with most extensive

failure in mitosis (blastoderm holes) don't have the highest levels of nuclear crowding (Figure 2P), or strongest asynchrony (Figure 2B), etc. Though, based on the quantifications and statistical significances we note that; one, severe mitotic failures (blastoderm holes) appear in a threshold-effect-like manner, appearing only in a fraction of embryos at 29°C; two, the nuclear crowding and asynchrony in nuclear cycles appears progressively as function of temperature, although the progression is not linear; and three, the fraction of embryos with large blastoderm holes best explains the increase in embryo lethality. Thus, we hypothesize a hierarchy of the defects, purely based on the fraction of embryos in which they appear as a function of temperature: exposure to elevated temperature will increase the frequency of mitotic failures as primary defect; nuclear crowding and nuclear cycle asynchrony will secondarily dictate the distribution of mitotic failures, producing extensive mitotic failures (blastoderm holes) as the ultimate effect in a fraction of embryo; eventually leading to a reduction in embryo fitness and an increase in embryo lethality.

Regions of embryo with greater nuclear crowding and with delayed nuclear cycles are associated with greater frequency of mitotic failures.

To test whether nuclear crowding and nuclear cycle asynchrony could influence the propensity of mitotic failures, we decided to compute the fraction of mitotic failures occurring in the regions of the embryo that had nuclear crowding and/or delayed nuclear division cycles. We constructed regions of the embryo with maximum nuclear crowding (crowded regions), maximum delay in nuclear division cycles (delayed regions), and a combination of crowded and delayed regions (combined region) (see methods).

We defined the crowded regions (Figure 3A), and delayed regions (Figure 3B) based of the distribution and dynamics of nuclei in live imaged embryos. Then, we overlayed the map of mitotic failures on the crowded regions (Figure 3C), delayed regions (Figure 3D), and the combined regions (Figure 3E). The crowded and delayed regions had rather comparable areas across temperatures (Figure 3F, G), indicating that any difference in the fraction of mitotic defects would be solely due to the nuclear crowding or due to the delays in nuclear cycles. Interestingly, the areas of the combined regions were smaller at elevated temperature (Figure 3H), indicating that there was an increase in the overlap between the crowded and delayed regions, and that we should expect a similar reduction in the fraction of mitotic failures, if the mitotic failures were distributed randomly.

The fraction of mitotic failures in crowded region increased progressively as function of temperature, reaching statistical significance for comparison between 22 and 29°C (Figure 3I), while the fraction of mitotic failures in delayed regions did not increase progressively, showing an abrupt increase from 28 to 29°C with only marginal statistical significance (Figure 3J). Interestingly, we see that the smaller area fractions in the combined regions correspond to even greater fraction of mitotic failures (Figure 3K). Additionally, the distribution of the fraction of mitotic failures in the combined region was unimodal, in contrast to the bimodal distribution of mitotic failures themselves (Figure 1G). Thus, we conclude that the combinatorial effect of nuclear crowding and asynchrony significantly increases the propensity of mitotic failures. We would further argue that nuclear crowding has a stronger impact on the propensity of mitotic failures than that due to nuclear cycle asynchrony.

Taken together, we find large clusters of defective mitosis and subsequent loss of nuclei in the center of about 10-20% of embryos developing at 29°C (Figure 1G). Nuclear crowding and nuclear cycle asynchrony cooperate to produce "hot spots" of mitotic failures (Figure 3). The aggregated

296 losses of nuclei in the center of the embryo persist until the end of blastoderm formation and leads
297 to visible holes in the newly formed embryonic epithelium (Figure S1). These holes indicate a severe
298 disruption in epithelial integrity and approximately match the increased rate of embryonic lethality
299 for development at 29°C (Figure 1B). Going further, we attempted to rescue the embryo lethality
300 defect using over-expression of various candidate genes, and if a rescue was possible, further
301 decided to quantify whether the rescue could be explained through fraction of mitotic failures in the
302 crowded region and the combined region.

303 **Identifying temperature-sensitive vulnerabilities in a deeply conserved cellular process**

304 The analysis of early fly development at moderately elevated temperatures, in our experiments, has
305 uncovered the first three hours of fly development as sensitive to environmental perturbations,
306 which can affect embryo fitness and increase embryonic lethality at elevated temperatures. This
307 increase in embryonic lethality correlates with specific perturbations in fundamental nuclear
308 dynamics, i.e., the timing and fidelity of nuclear divisions within the spatial constraints of a cortex
309 densely packed with nuclei. To address how a deeply conserved and presumably robust process like
310 mitosis could be affected so dramatically at a temperature lower than those eliciting a heat-shock
311 response, we functionally probed for possible vulnerabilities in core molecular interactions that
312 control nuclear dynamics in the early fly embryo.

313 In stark deviation from canonical cytokinesis, cortical nuclear divisions in the syncytial fly embryo
314 rely on cell polarity cues that are set up at shallow metaphase furrows of the egg cortex, where they
315 orient mitotic spindles parallel to the cell surface (A. Schmidt and Grosshans 2018; Xie and
316 Blankenship 2018). What's more, these furrows are transient, and are reestablished during each
317 nuclear cycle: including new growth of membrane between nuclei, reestablishment of cell polarity,
318 along with reorganization of cytoskeletal elements. The dependence on transient membrane
319 invaginations to establish cell polarity information represents the least conserved and potentially
320 most labile element of cortical nuclear divisions in insect embryos. To test whether the fidelity of
321 cortical mitoses at elevated temperatures hinges upon insufficiently robust cell polarity signaling, we
322 overexpressed two known prominent polarity proteins, Bazooka (baz, a Par-3 homolog) and Disks-
323 large (dlg) (Harris and Peifer 2004), and asked whether we rescue embryo lethality defect, and the
324 increase in the fraction of mitotic failures in crowded regions and in combined regions with
325 combinatorial effect of nuclear crowding and asynchrony.

326 When we over-expressed either *baz* or *dlg* we did not see a significant change in embryo lethality at
327 control temperature (25°C) as compared to the control (Figure 4A). The lethality was greater in
328 outcross controls at elevated temperature (29°C) similar to results in previous experiments, while
329 the embryos over-expressing either *baz* or *dlg* faired significantly better at the elevated temperature
330 (Figure 4A). We note however that the rescue of lethality at elevated temperature in *baz* over-
331 expressing embryos was only marginally significant, with a lot of variability between samples.
332 Additionally, *dlg* over-expressing embryos at normal temperature showed higher variability in
333 embryo lethality than their outcross control counterparts. Consistent with these results, *baz* over-
334 expression did not rescue the increase in the fraction of mitotic failures, neither in the crowded
335 regions, nor in the combined regions at elevated temperature (Figure 4B, C), though the large
336 blastoderm holes were absent in these embryos. Then, *dlg* over-expression rescued the increase in
337 fraction of mitotic failures only in the crowded region at elevated temperature (Figure 4B, C), though
338 the large blastoderm holes were absent in these embryos. Additionally, *dlg* over-expression

339 increased the fraction of mitotic defects at normal temperature in both, the crowded region and in
340 the combined region, occasionally producing small blastoderm holes (Figure 4B, C).

341 Above results indicated a temperature-dependent vulnerability more specific to the molecular core
342 of the mitotic spindle rather than its setup in the context of a syncytial embryo. To faithfully pull
343 sister chromatids towards the actin cortex on either side of the division plane, the execution of
344 mitosis relies on tightly regulated interactions between the actin cortex and the microtubules of the
345 mitotic spindle (Cao et al. 2010; Rizzelli et al. 2020). In Drosophila, these critical interactions of actin
346 and microtubules have been associated with a complex of three proteins: α-Catenin (αCat), which
347 binds to the actin cortex; β-Catenin (βCat, or armadillo in Drosophila), which binds to α-Catenin; and
348 Adenomatous polyposis coli 2 (Apc2), which links to β-Catenin and binds the microtubules of the
349 mitotic spindle (McCartney et al. 2001). Within this tripartite complex, the interaction of αCat and
350 βCat is direct and presumably non-regulated, whereas the interaction of βCat and Apc2 is mediated
351 by a specific kinase, the Drosophila homolog of the Glycogen Synthase Kinase 3β, Shaggy (sgg) (Rim,
352 Clevers, and Nusse 2022). Additional indication for the activity of the complex came when we fixed
353 and stained embryos developing at elevated temperature, to visualize nuclei and cortical F-actin (see
354 methods). We could observe F-actin structures in embryos at elevated temperature (Figure S9, see
355 panel F), which were reminiscent of those in embryos mutant for *Apc2*, β*Cat*, or *sgg*, as previously
356 described (McCartney et al. 2001). Thus, we hypothesized that boosting the activity of the complex
357 through over-expression of one or more of its components should meaningfully rescue the embryo
358 lethality defect, and the increase in the fraction of mitotic failures in crowded regions and in
359 combined regions.

360 To test whether the fidelity of cortical mitoses at elevated temperatures was affected by
361 insufficiently tight or poorly controlled coupling of actin and microtubules, we overexpressed either
362 *αCat* or *sgg*, and again asked whether the increase in embryo lethality at elevated temperature was
363 rescued. When we over-expressed either *αCat* or *sgg* we did not see a significant change in embryo
364 lethality at control temperature (25°C) as compared to the control (Figure 4D). The lethality was
365 greater in outcross controls at elevated temperature (29°C) similar to results in previous
366 experiments, while the embryos over-expressing either *αCat* or *sgg* faired significantly better at the
367 elevated temperature (Figure 4D). Consistent with these results, both *αCat* and *sgg* over-expressions
368 rescued the increase in the fraction of mitotic failures, in the crowded regions, as well as in the
369 combined regions at elevated temperature (Figure 4E, F), with the large blastoderm holes absent in
370 these embryos. These results suggested that an experimental strengthening of actin binding was
371 able to attenuate temperature-dependent destabilizations of the mitotic spindle. These findings are
372 consistent with the idea that the scaffolding activity of αCat, βCat, and Apc2, mediated by sgg,
373 constitutes a thermosensitive controller of nuclear division fidelity in the early blastoderm embryo.

374 Given the reduction in mitotic fidelity at elevated temperature, we were wondering whether any
375 regulator of mitosis could rescue temperature defects upon overexpression. To test this possibility,
376 we tested other regulators of mitosis and focused on the activity of mud and insc. In epithelia, the
377 activity of 'Mushroom body defect' (mud, NuMA homolog) and that of Inscuteable (insc) is known to
378 dictate the orientation of mitotic spindle during cell division (Mapelli and Gonzalez 2012). Similar
379 activity might be present for nuclear divisions during syncytial blastoderm stage, raising the
380 possibility that over-expression of *mud* or *insc* could rescue embryo lethality, presumably through
381 reducing mitotic failures. However, neither of the over-expressions ameliorated the increased
382 embryo lethality at elevated temperature, with mud over-expression additionally increasing the

383 lethality at normal temperature as well (Figure S11). This failure to rescue embryo lethality further
384 allowed us to argue that, the elevated temperature critically challenges the core machinery of
385 mitotic spindle, more so than the regulation of spindle orientation.

386 **The natural distribution of a few regulators of spindle dynamics varies along thermoclines.**
387 Our analyses show how elevated temperatures during the first hours of fly development affect early
388 embryonic cell biology; it may seem suggestive, but it was not shown that naturally occurring
389 changes similar to our overexpression of cytoskeletal regulators could shape the evolution of fly or
390 insect development in general. To address this possibility more directly, we analyzed the distribution
391 of standing genetic variations associated with the regulation of the spindle dynamics (combination
392 of GO terms, cell polarity, spindle organization, and spindle localization), and tested the hypothesis
393 that such variation was randomly distributed with respect to described thermoclines, i.e., continent-
394 scale gradients of annual mean temperature. We found that indeed, most standing genetic variation
395 associated with putative spindle dynamics regulators was distributed without a clear thermoclinal
396 pattern, although the fraction of genes showing clinal distribution was greater than those associated
397 with a more generic GO term like 'metabolic process' (Figure 4G, Table S1, S2). A clear and notable
398 outlier in this analysis was *sgg*, which was marked with a north/south clinal distribution of natural
399 variations independently in populations in the US, in Europe, and in Australia (see also, Table S3).
400 These findings strongly suggest that the thermosensitivity that *sgg* exhibits in lab conditions,
401 constitutes a biological property that can be exposed and selected for also in natural populations
402 and during the course of evolution. Similarly, we found that 'scribble', a cell polarity protein which
403 interacts with dlg (Khoury and Bilder 2020; 2022), was also clinal in all 3 populations. Further
404 experiments are required to formally test the possibility of a rescue of embryo lethality with over-
405 expression of *scribble*, which will be addressed in future experiments.

406 **Discussion:**

407 **Cellular basis of the sensitivity against elevated temperature during early embryonic development**
408 With our work, we demonstrate how the first hours of embryonic development are vulnerable to an
409 exposure to a non-heat-shock temperature. We identify the mechanistic basis for this vulnerability:
410 it is the interaction between microtubules and F-actin during mitosis is thermolabile. Given that
411 these early processes till blastoderm formation are conserved across insects (Lynch, El-Sherif, and
412 Brown 2012; Lemke, Kale, and Urbansky 2020), our results implicate a vulnerability in a plethora of
413 insect species. It would be interesting to investigate whether mechanisms exist in nature to
414 accommodate for this vulnerability. In the backdrop of this sensitivity, it is the challenge for the
415 embryo to establish an egg cortex that is uniformly populated with cortically anchored nuclei that
416 carry positional information for subsequent steps of epithelial morphogenesis and cell
417 differentiation. A defect in these early morphogenetic processes and cell differentiation could lead
418 to defects in subsequent processes, ultimately leading to developmental failure and embryo
419 lethality. Thus, with our data, a mechanism emerges to establish the link between the proximate
420 effects of elevated temperature on cytoskeletal regulation, and its ultimate impact on the survival of
421 embryos.

422 What is the best predictor of lethality in embryos exposed to elevated temperatures? In our analysis,
423 we found 3 defects in embryos at elevated temperature: mitotic failures, nuclear crowding, and
424 nuclear cycle asynchrony. Mitotic failures, especially during the last mitosis prior to cellularization,
425 can lead to loss of nuclei, and consequently a loss of local positional information that is advected

426 and lost with the nuclei. This can lead to missing cell fates in the coordinate system of the embryo,
427 leading to missing embryonic structures, which can pose challenges for developmental fidelity.
428 Comparing the fraction of dead embryos at elevated temperature vs. the severity of mitotic failures,
429 we would argue that the embryos with the most severe mitotic failures, i.e., those that end up with
430 holes in blastoderm epithelium, are the ones that don't hatch into larvae. In our over-expression
431 conditions, it is clear that the severe mitotic failures (blastoderm holes) are absent in the genotypes
432 that rescue the embryo lethality at elevated temperature. It remains to be seen if an extensive, but
433 scattered, loss of nuclei poses any developmental disadvantage to the embryo or not. It is possible
434 that such disadvantages might be apparent only during larval stage, and might directly affect larval
435 fitness, but our current analysis wouldn't capture that effect. Additionally, developmental
436 robustness can vary between species, which raises the possibility that not all fly species will be able
437 to accommodate such developmental disadvantages. Further, here we have presented 28 embryos
438 of control genotype at elevated temperature, of which 6 have large- and 5 have small blastoderm
439 holes. In all of these cases, the blastoderm holes appear in the region where we see an overlap
440 between nuclear crowding and the delay of nuclear divisions. Thus, we further argue that the severe
441 version of the defect at elevated temperature (blastoderm holes) occur where the three phenomena
442 (mitotic failures, nuclear cycle asynchrony, and nuclear crowding) spatially overlap. Thus, even
443 though all of the 3 defects can independently reduce embryo fitness, we demonstrate that the
444 defects cooperate, to induce lethality in a fraction of embryos.

445 **Genetically increasing robustness of early embryos against environmental perturbations**
446 In theory, the robustness of embryonic development can be higher depending on, say, the quality of
447 the food available to the mother. Thus, one can hypothesize a rescue of embryonic lethality at
448 elevated temperature through, e.g., improvement of the quality of the diet available to the adult
449 females. A previous study compared the effect of temperature and the atmospheric O_2 levels on
450 embryo survival, where they report consistently greater embryo survival at 25% Oxygen
451 concentration, than the normal 21% (Kuntz and Eisen 2015). These results indicate that it might also
452 be possible to increase the robustness of embryo development through increasing the atmospheric
453 O_2 concentration. However, such solution might not be heritable, and might not confer an increase
454 in future fitness. Previous studies have increased embryo survival in face of exposure to elevated
455 temperature through over-expression of heat-chock proteins (Lockwood, Julick, and Montooth
456 2017). Presumably, this increases the capacitance of the system to tolerate environmental insults,
457 akin to how heat-shock proteins are known to act as capacitors for genetic variation (Rutherford and
458 Lindquist 1998; Sangster, Lindquist, and Queitsch 2004). However, such a rescue would not shed
459 light on underlying biology of temperature defects, as the effect of such perturbations on the mitotic
460 failures would remain nebulous. Thus, to rescue the lethality at elevated temperature, we used our
461 cellular level understanding of the defects to guide our choice of candidate genes for genetic
462 manipulations. This approach additionally allowed us to challenge our cellular level understanding of
463 the defects at elevated temperature, as we construct and test hypotheses about the over-expression
464 of various genes towards a genetic rescue.

465 Various genotypes in our experiments, specifically the overexpression of *αCat*, *sgg*, *baz*, or *dlg*, act to
466 reduce one or more of the defects (embryo lethality, presence of blastoderm holes, fraction of
467 mitotic failure in crowded region, or that in the combined region) that occur due to exposure to
468 elevated temperature. Here, we would argue that *αCat* and *sgg* overexpression are the superior
469 experimental condition among these as far as potential for a rescue is concerned, as they produce

470 virtually no side-effects (unlike *dlg* overexpression at normal temperature), while robustly reducing
471 the lethality at elevated temperature (unlike *baz* overexpression). Additional support for this notion
472 comes from our analysis of the presence of natural variation along thermoclines, where we
473 identified *sgg* as an interesting candidate gene, along with *scribble*. The list of genes associated with
474 spindle dynamics (combination of GO terms spindle organization, spindle localization, and cell
475 polarity) included our candidate genes *baz*, *dlg*, *sgg*, *mud*, and *insc*. While *αCat* is not presently
476 associated with GO terms related to spindle dynamics, we also did not find it to be clinal in our
477 extensive literature search. It is possible that natural fly populations don't possess sufficient standing
478 genetic variation at that locus that could provide a selective advantage. In any case, an overlap
479 between our candidates and potential natural candidate genes increases our confidence in our
480 approach to mitigate the detrimental effects of an exposure to elevated temperature during early
481 embryonic development.

482 Given that both *αCat* and *sgg* overexpression show a robust rescue of embryo lethality, we would
483 further argue that the interaction between microtubules and cortical F-actin, as supported by the
484 tripartite protein complex between αCat, βCat, and Apc2, mediate by sgg, is sensitive to
485 temperature fluctuations. It is likely that the association/dissociation constants for one or more
486 binding interactions (F-actin with αCat, αCat with βCat, and βCat with Apc2) decrease/increase with
487 an increase in temperature. It is also likely that the kinase activity of sgg reduces with an increase in
488 temperature, hampering the association between βCat and Apc2. Further experiments are required
489 to test these ideas. However, here we also note that many nuclei manage to divide in embryos
490 mutant for βCat, Apc2, and sgg (McCartney et al. 2001), forming a somewhat defective blastoderm.
491 This would indicate presence of alternative mechanisms that can also be reinforced to increase the
492 robustness of mitosis, and identifying and testing such mechanisms would be of great interest to
493 rescue embryo lethality at elevated temperature.

494 **How fast can nature increase the robustness against the adverse effects of elevated temperature?**
495 A recent experiment (Rudman et al. 2022) indicates that nature might already be exploiting the
496 allelic plasticity in our candidate genes to increase robustness against elevated temperatures. In this
497 study, the researchers allowed fly populations to naturally evolve from spring through summer till
498 the fall season, and found that specific single nucleotide polymorphisms were selected for in the
499 regulatory regions of *sgg* and β*Cat*, along with many other genes. It is interesting to see that these
500 genes show selectable variation at the population level, and that an over-expression of *sgg* in our
501 analysis is capable of rescuing the embryo lethality at elevated temperature. To be clear, the study
502 does not comment on whether the accumulated mutations lead to an over-expression or
503 hyperactivation of *sgg*, and at the same time, the analysis won't pick up candidates that don't have
504 sufficient variation in the seed population. In any case, our functional analysis can be effectively
505 used to test for the function of any gene that rescues (or worsens) the effect of elevated
506 temperature on early embryonic development, in any fly embryo that's amenable to experimental
507 manipulations. We believe that our experimental pipeline holds the promise to uncover exciting
508 biology, while understanding how physiological processes are affected by the exposure to elevated
509 temperature.

510 **Sensitivity of early embryonic development to the global warming and climate change**
511 Climate change is a global problem that threatens the existence of life on earth as we know it (IPBES
512 2019). Given the gigantic scope of the problem, it is overwhelming to address the question in its
513 entirety. Instead, we can breakdown the problem into manageable pieces, in accordance with our

area of expertise, and address them to the best of our abilities. In this context, we decided to focus on effect of elevated temperature on the physiology of flies, given their vital roles for the functioning of ecosystems (Raguso 2020). In our efforts to understand the effects of global warming, we focused on the early embryonic development in *Drosophila*, which we found to be especially sensitive to exposure to elevated temperature. Here, we identified the syncytial blastoderm stage during embryonic development as the earliest possible time window that's sensitive to elevated temperature. We could also observe cascading defects in the cellular blastoderm formed thereafter. An increase in embryonic lethality, due to the early exposure to elevated temperatures, further indicated that, presumably, the subsequent developmental processes are affected as well. We also see a small increase in embryonic lethality when we expose post-cellularization embryos to elevated temperature, indicating additionally that the temperature sensitive time window might actually be longer than just the pre-gastrulation developmental phase. It is easy to imagine that, in wild, embryos would be exposed to elevated temperature for first few hours, starting form egg lay till well beyond gastrulation. Given that these early processes during the embryonic development are conserved across fly species (Lemke, Kale, and Urbansky 2020), our results raise the possibility that many other key species, would exhibit similar defects during early embryonic development, will have an increase in lethality, and will be overall threatened due to global warming. It is rather impressive that an exposure to a non-heat-shock temperature during first few hours of embryonic development is capable of reducing the fitness of the entire embryonic development to increase embryonic lethality: an effect which is presumably conserved across the animal kingdom, and would be worth exploring at cell biological level to improve embryo survival. Perhaps, the temperature sensitive developmental window is so crucial as it includes gastrulation, very much in agreement with the famous quote from Lewis Wolpert, "It is not birth, marriage, or death, but gastrulation which is truly the most important time in your life".

539 **Materials and methods:**

540 Fly lines and genetics:

541 *OregonR* line was used as WT *Drosophila*.

542 *Histone-RFP* expresses RFP tagged version of His2Av. Insertion on 3rd chromosome. Bloomington
543 #23650.

544 *Jupiter-GFP* expresses GFP tagged version of microtubule binding protein Jupiter. Insertion on 3rd
545 chromosome. Always used in combination with *Histone-RFP*. Gift from Jan Felix Evers.

546 *67-Gal4* (mat αTub-GAL4-VP16) is a maternal specific Gal4 driver. Insertion on 2nd chromosome.
547 Always used in combination with *Histone-RFP* and *Jupiter-GFP* in the over-expression experiments
548 (see below). Gift from Thomas Lecuit.

549 The following lines were used to drive the over-expression of various genes of interest in an attempt
550 to rescue the effects of elevated temperature. *baz*, Bloomington #17613; *dlg*, Bloomington #15779;
551 *αCat*, Bloomington #65590; *sgg*, Bloomington #15886; *mud*, Bloomington #22371; *insc*, Bloomington
552 #39676. An outcross to *w1118* was used as control.

553 For various over-expression experiments, we first crossed virgins from the Gal4 line '+; 67-Gal4;
554 Jupiter-GFP, Histone-RFP' to the males of over-expression line 'UAS-X; +; +' (X= *baz*, *dlg*, *sgg*, or *mud*)
555 or '+; +; UAS-Z' (Z= *αCat*, or *insc*), or to males of *w1118* as control. F1 virgin females from these
556 crosses were back crossed to males of the same paternal genotype.

557 Genotypes associated with various figure panels are listed in Table S3.

558 Embryo collection: For any experiment, we put males and females of appropriate genotypes into
559 transparent cylindrical embryo collection cages, with inner diameter of ~5cm. Fine wire mesh is
560 glued to top side of the cage to allow air exchange while keeping the flies trapped, while the bottom
561 of the cage is closed with apple-juice agar plates, with a thin layer of yeast paste, which is where flies
562 deposited the embryos. To prepare the agar plates, we typically prepare 1l of apple-juice agar
563 solution. For this, we boiled 24gm of agar in 750ml of water, to which we added 250ml of fresh
564 store-bought apple juice, while stirring on a hot plate. We make the final amount of sucrose to
565 25gm: the amount of additional sucrose depends on the sugar content of the apple juice. This
566 solution is sufficient for ~80 petri-dishes of 6cm diameter. After agar is solidified, the plates can be
567 stored for long time at 4°C. Before the embryo collection, the plates were covered with a thin layer
568 of yeast paste (to stimulate oviposition), and were pre-incubated to the embryo collection
569 temperature depending on the temperature regimen, for at least half an hour. *Drosophila* females
570 are known to hold onto the embryo long after fertilization, such that a large part of the early embryo
571 development can occur inside the abdomen. To avoid these embryos, we perform a sham embryo
572 collection for about an hour, from which all embryos are discarded. Following this sham collection,
573 we collect the embryos that are actually used in the experiment.

574 Embryo lethality experiment: There were 3 temperature regimes in the embryo lethality
575 experiments, as depicted in Figure 1A. Depending on the regimen, we collected embryos for 1 hour
576 either at normal temperature (24-25°C) or elevated temperature (29-30°C). The 24-25°C collections
577 (corresponding to normal temperature) were done on the bench top. The 29-30°C collections
578 (corresponding to elevated temperature) were done in a water bath, where the bottom surface of
579 the embryo collection agar plate is in thermal contact with the heated water. For NN or EN, we

580 collected embryos for 1 hour either at normal temperature or elevated temperature, and then
581 incubated them at the same temperature for another 2 hours. Afterwards, the embryos are washed
582 with bleach for 10-15 seconds, then washed thoroughly with tap water, aligned on a 24x60mm
583 rectangular coverslip, and covered with halocarbon oil. For NE, we collected embryos for 1 hour at
584 normal temperature, and then incubated them at the same temperature for another 1.5 hours.
585 Within the next half an hour, the embryos are washed with bleach for 10-15 seconds, then washed
586 thoroughly with tap water, aligned on a 24x60mm rectangular coverslip, and covered with
587 halocarbon oil. Then, we incubated them at elevated temperature for 3 hours. Then, for all the
588 temperature regimen, the coverslips with embryos were incubated at normal temperature for about
589 a day, following which we counted the number of eclosed larvae, and the number of dead embryos.
590 The embryonic lethality was estimated as the percentage of dead embryos, i.e., 100*(number of
591 dead embryos)/ (number of dead embryos + number of larvae). We excluded the unfertilized
592 embryos from these calculations.

593 Embryo fixation and Imaging: We used 2 different temperature regimens for embryo collection for
594 fixation and staining. We collected embryos for 3-4 hours either at normal temperature (24-25°C) or
595 elevated temperature (29-30°C). The 24-25°C collections (corresponding to 25°C regimen) were
596 done on the bench top. The 29-30°C collections (corresponding to 29°C regimen) were done in a
597 water bath, where the bottom surface of the embryo collection agar plate is in thermal contact with
598 the heated water. Afterwards, the embryos are washed with bleach for 40-45 seconds, then washed
599 thoroughly with tap water, and then fixed immediately. Collecting embryos for longer duration is not
600 a problem here, as we only image and analyze the embryos that are before gastrulation stage,
601 through post hoc staging and sorting. Here, we did 2 kinds of experiments; one, where the aim was
602 visualizing the nuclei from the entire embryo (data in Figure S2); and two, where the aim was
603 visualizing the nuclei along with F-actin distributions from half embryos (data in Figure S9).
604 Accordingly, we used 2 different protocols for embryo fixation, staining, mounting, and imaging.

605 In the experiment where we wanted to *visualize all nuclei from the entire embryo*, we used heat
606 fixation, and stained the embryos with DRAQ5. Briefly, we transferred the processed embryos to
607 50ml tubes with a brush, and drained the excess water. To this tube, we added the boiled-to-
608 turbidity heat-fix solution (28% 500µl NaCl + 5% 200µl TritonX100 + 19.3ml water), incubated it for
609 ~20sec with thorough mixing, and then immediately added water to cool down the mixture. Then,
610 we transferred the fixed embryos to 2ml microfuge tubes, sequentially added n-Heptane and
611 methanol in equal proportions, vigorously shook the tube for about half a minute to break-open and
612 remove the vitelline membrane. This was followed by 3x washes of methanol. Here, we started the
613 staining immediately after, although the embryos can be stored in methanol for long time. The
614 embryos were rehydrated with PBT (0.01% solution of Tween20 in PBS) over 3 washes, following this
615 we stained the embryos with 1:1000 DRAQ5 for 1 hour. Afterwards, we washed the embryos 6x with
616 PBT, re-suspended them in 3:1 glycerol:PBS solution, and mounted them between 2 rectangular
617 coverslips. The spacing between the coverslips was optimized to keep the embryos in place w/o
618 deforming them. Then we imaged the embryos through both coverslips, and stitched the two half
619 embryos during image analysis to get the full view (see below). Images were acquired on Leica SP8
620 DMi8 inverted confocal microscope using 20x glycerol objective (0.75NA), with 1.15x digital zoom, at
621 1µm step-size in z, and a final x-y resolution of 0.247 µm/pixel.

622 In the experiment where we wanted to *visualize the nuclei and F-actin*, we used formaldehyde
623 fixation, and stained the embryos with DAPI and Phallacidin. Briefly, we transferred the processed

embryos to 20ml vial with a brush, which contained the fixation mix (3500µl PBS + 37% 1000µl formaldehyde + 4500µl n-Heptane). The vial was shaken on a platform shaker for 25 minutes @200rpm. Then, we transferred the fixed embryos to 2ml microfuge tubes, sequentially added n-Heptane and 90% ethanol in equal proportions, vigorously shook the tube for about half a minute to break-open and remove the vitelline membrane. This was followed by 3x washes of 90% ethanol. Here, we started the staining immediately after, although the embryos can be stored in 90% ethanol for a week or so. The embryos were rehydrated with PBT (0.01% solution of Tween20 in PBS) over 3 washes, following this we stained the embryos with 1:1000 DAPI for 1 hour, followed by 1:500 Phallacidin for 1 hour. Afterwards, we washed the embryos 4x with PBT, re-suspended them in 3:1 glycerol:PBS solution, and mounted them between 2 rectangular coverslips, followed by imaging. Images were acquired on Leica SP8 DMi8 inverted confocal microscope using 20x glycerol objective (0.75NA), with 1.2x digital zoom, at 1µm step-size in z, and a final x-y resolution of 0.473 µm/pixel.

Embryo Live imaging: We used 4 experimental temperature regimes for embryo live imaging. We collected embryos for 1 hour either at normal temperatures (22-23°C, 24-25°C, or 27-28°C) or elevated temperature (29-30°C). The 22-23°C collections (corresponding to 22°C imaging) were done in the fly incubator. The 24-25°C collections (corresponding to 25°C imaging) were done on the bench top. The 27-28°C collections (corresponding to 28°C imaging) or the 29-30°C collections (corresponding to 29°C imaging) were done in a water bath, where the bottom surface of the embryo collection agar plate is in thermal contact with the heated water. Afterwards, the embryos are washed with bleach for 35-40 seconds, then washed thoroughly with tap water at the same temperature as embryo collection. We then aligned the embryos on a 25mm diameter circular coverslip, covered them with halocarbon oil, and immediately transferred them to the temperature controller setup on the microscope that's pre-equilibrated to the experimental temperatures for normal temperature regime, (22, 25, or 28°C) or the elevated temperature regime (29°C). We used the temperature controller setup from Warner instruments (locally supplied by MultiChannelSystems). The setup consists of; QR-40LP, which holds the 25mm coverslip with embryos; QE-1HC, which heats/cools QR-40LP along with the embryos mounted in it; LCS-1, the liquid cooling system that isolates the QE-1HC from the effect of ambient temperature; and CL-100, the bipolar temperature controller that can impart the temperature of interest against the baseline set by LCS-1. We mounted QE-1HC on the microscope stage, with LCS-1 and CL-100 as the peripherals controlling the temperature. Images were acquired on Leica SP5 DMI6000CS inverted confocal microscope using 40x water objective (1.1NA), with 1x digital zoom, at 2µm step-size in z with 20 z-steps overall, and a final x-y resolution of 0.379 µm/pixel. As mentioned in the main text, we acquired images starting from interphase 10 or before, till the beginning of gastrulation movements. We recorded the timelaspe at a frame rate of 1 frame every 30sec, 1min, or 2min depending on whether we recorded at a time 1, 2, or 3-4 embryos in parallel.

Image analysis and statistics: All image analysis was done using FIJI freeware. There are 7 different kinds of image analyses presented in the manuscript. These are; one, whole embryo reconstruction to see distribution of nuclei in the entire embryo (fixed embryos); two, the analysis of mitotic failures (live embryos); three, the analysis of nuclear movements (live embryos); four, analysis of nuclear cycle asynchrony (live embryos); five, analysis of nuclear crowding (live embryos); six, analysis of the fraction of mitotic failures (live embryos); and seven, comparing the distribution of nuclei alongside that of F-actin (fixed embryos). All the statistical analysis was done using Prism 9 (GraphPad). This includes, the curve fitting (see below, the analysis of nuclear crowding), estimating

668 the non-parametric statistical significances, and estimating the 95% confidence intervals (CI) on the
669 medians. The straight-line fits for analysis of nuclear movements were done using ImageJ macro
670 language.

671 In the analysis to *reconstruct the nuclear distribution in the whole embryo*, we used a custom-built
672 image analysis pipeline to fuse the halves of the same embryo, followed by the computing the
673 distance of each point inside the embryo from the embryo surface. Here we refer to the two views
674 of the embryo as "half embryo", even though in reality the volume in either "half" spans about 70-
675 75% of the embryo width, providing a significant overlap between the two halves. In the pipeline, we
676 process the raw images, stitch the two half embryos, render the fused embryo in lateral view,
677 segment the embryo volume, and then segregate the nuclei as a function of their distance from the
678 surface of segmented embryo volume. First, we processed the raw images: to improve visualization
679 of the nuclei, we used 'Minimum 3D' filter with radii x=y=1, and z=3, and to reduce noise, we used
680 'Median 3D' filter with radii x=y=z=1. Then, we homogenized the brightness/contrast between the
681 two half embryos. Following these steps, we manually aligned the half embryos along their AP axis,
682 and then used the BigWarp (Bogovic et al. 2016) package in the BigDataViewer ecosystem (Pietzsch
683 et al. 2015) to align the half embryos using manually selected interest points. Essentially, we
684 selected either subcortical- or yolk-nuclei that could be identified in both half embryos. We further
685 cropped the output images to keep only a small margin around the embryo with "aligned halves", in
686 order to reduce the computational load in the steps to follow. After the manual alignment step, we
687 used BigStitcher (Preibisch, Saalfeld, and Tomancak 2009) to further align embryo, using phase
688 correlation method, to produce the "fused embryo". In case of many embryos, additional manual
689 transforms were necessary to produce a fused embryo that passes visual inspection. The fused
690 embryos were then rotated as necessary, and resliced to produce lateral views. Following this, we
691 processed the fused embryo to separate the regions of embryo that contain cortical-, subcortical,
692 and yolk-nuclei. First, we used the nuclear signal to segment the embryo volume, using simple
693 thresholding. This generated a binary image that corresponds to the embryo volume. Then using '3D
694 Distance Map' (a plugin in the 3DSuite), we compute the Euclidian distances in 3D, i.e., for each pixel
695 inside the embryo gets the grayscale value corresponding to its distance from the embryo surface.
696 All pixels with Euclidian distance <10µm would be considered as the cortical layer, those within
697 range of 10-30µm would be consider subcortical, and those farther than 30µm from embryo surface
698 would be considered as part of the yolk region. These distances are determined empirically, using
699 approximate measurements from various fused embryos. Typically, nuclei have the diameter of 5-
700 10µm depending on the phase of nuclear division cycle, while the cell height at the end of
701 cellularization is about 30µm. The pixels in these regions were then color coded and presented as
702 either as maximum projections or cross-sectional views in Figure S2.

703 In the *analysis of mitotic failures*, we tracked expelled nuclei back in time to identify the mitosis
704 when they were born, and to categorize the expulsion as pairwise or isolated (see examples
705 respectively in Figure 1F and Figure S3D). We considered a nucleus to be expelled, if its apical-most
706 tip was at least 12µm away from the embryo surface. To simplify the identification of expelled
707 nuclei, we color-coded the Histone-RFP signal as a function of distance from the embryo surface.
708 This is similar to above analyses, except we use the 'LocalZPojector' plugin in FIJI (Herbert et al.
709 2021) to define the distance from the embryo surface, while to predict the embryo surface itself we
710 use the Jupiter-GFP signal, which was co-imaged with Histone-RFP. Thus, first we color-code the

nuclei, and then manually identify and count the number of pairwise or isolated nuclear expulsions during interphase 14.

In the *analysis of nuclear movements*, we manually tracked the entire progeny of a few nuclei, starting from the mother nucleus in late interphase 10 till the 8 great-granddaughter nuclei till late interphase 13. Having assigned all of these nuclei to a single cluster, we can then calculate the center of the cluster at each time point. We chose nuclei along one continuous row at interphase 10, and tracked their progeny in their individual clusters. For sake of simplicity and consistency, we only chose those nuclear clusters whose entire progeny can be tracked, i.e., we can follow the cluster and see the formation of all 8 great-granddaughter nuclei in interphase 13. This way, we obtained ≥ 13 clusters in any embryo that we tracked. For each of these nuclear cluster trajectories, we fitted a straight-line to coordinates for the center of the cluster, over time (dashed lines in Figure S5B). Then, we calculated the distance of the center of the nuclear cluster to this line at every timepoint. An average of these distances over a specific time period was used as an estimate for deviations in the center of nuclear clusters over that time period. We observed that the clusters move significantly starting from anaphase till a few minutes into the subsequent interphase, as the clusters return to their normal position. Thus, we decided to separately analyze these periods of extensive movement vs. the periods when the cluster movement is low. To identify the periods of extensive movements consistently and objectively, we noted that these movements start at least 1 timepoint (30 sec) before we see the first telophase in any of the tracked clusters, while the movements mostly subside within 3 minutes after all of the nuclear clusters have finished telophase. Thus, we defined the window of extensive movement as starting from 30 sec before appearance of first telophase nuclei, till 3 min after the appearance of last telophase nuclei. Once we have an objective definition of various time periods, it is straightforward to calculate the average deviation in the center of nuclear clusters.

In the *analysis of asynchrony in nuclear cycles*, we marked various timepoints in the timelapse recordings to follow the progression of nuclear cycles in the anterior-, middle-, and posterior-5th of the field of view. For sake of simplicity, we marked the transitions from a telophase 13 to interphase 14, i.e., the first timepoint when the daughter nuclei in any region go from telophase 13 to interphase 14. If the timepoint for this occurance in the anterior is 'T_a', that in posterior is 'T_p', while the same in the middle is 'T_m', then the 'asynchrony' can be calculated as,

$$asynchrony = T_m - \left(\frac{T_a + T_p}{2}\right)$$

Essentially, we start with the expectation that T_m should be the average of T_a and T_p (maximum synchrony), and a deviation from this expected value would be the asynchrony. Figure S7 diagramatically demonstrates this analysis.

In the *analysis of nuclear crowding*, we analyzed the distribution of nuclei at the end of interphases, as that's the time when the distribution is as stable as it can be. To assess nuclear crowding, we started with segmentation of nuclei in the field of view. Here, we used the 'Find Maxima' command to identify local intensity maxima, and imprinted those on an image. Many of these maxima marked a nucleus. We did manual corrections to, remove the maximum that didn't correspond to a nucleus, add a maximum for nucleus that didn't have a maximum associated with it, or correct the maxima that were too off-center from corresponding nuclei. Then we used Voronoi tessellation to mark territories around these maxima to generate pseudo-cells. We excluded territories that, touched the

edge of the image, that had aberrant shapes (aspect ratio>2), or those with aberrant pixel intensities (pseudo cell containing pixels with <5 units of intensity, typically the case with ill-defined pseudo-cells at the edge of segmentation). Thus, each nucleus is associated with a pseudo-cell area value ('Area' in μm^2), and an x-coordinate value for the center of the pseudo-cell ('X' in µm) (x-axis of the image aligned with anterior-posterior axis of the embryo). We fitted these with the equation of a parabola such that 'Area' can be expressed as a function of 'X',

$$Area = aX^2 + bX + c$$

Here, the curvature of the parabola will be higher in case of greater nuclear crowding (compare Figure 2L-O). Thus, the fit parameter 'a', which dictates the curvature of the parabola, was used to estimate the extent of crowding.

In the *analysis of the fraction of mitotic failures*, we tracked expelled nuclei back in time same as the analysis for mitotic failures, except now we also recorded where the nuclei were lost from, to get a map of the distribution of mitotic failures. In parallel, we generated regions in the embryo that correspond to maximum nuclear crowding, maximum delay in nuclear divisions, and a combination of the two regions. To have an objective definition of the area of maximum crodwing we looked to a previous study on the effect of nuclear density on nuclear division cycles (Lu et al. 2009). This study indicates that the nuclear division cycles seize when the embryo reaches ~70% of the normal cellularization nuclear density. Another previous study reported the nuclear domain area (i.e., the pseudo-cell area) to be 28.8 μm^2 at cellularization (Telley et al. 2012). We corroborate this number with our own quantifications (data not shown). Thus, for simplicity of calculations, we assume that *Drosophila* embryos have 6000 nuclei at interphase 14 each with a area of 29 μm^2. The a 70% density of nuclei would thus correspond to 4200 nuclei at interphase 14, each with an area of 41.43 μm^2, which we approximate to 42 μm^2. Thus the back of the envelop calculation indicated that nuclei will seize to divide when their pseudo-cell area drops below ~42μm^2. We observed that in embryos developing at 29°C, the central regions of the embryo contained many nuclei that had pseudo-cell areas less than 42μm^2, even at interphase 13. Thus, we used this criterion to define areas of embryos that have likely reached the 70% cellularization nuclear density, at one nuclear division cycle earlier, albeit only locally. Since the embryos at normal temperatures (22, 25, and 28°C) rarely have nuclei with pseudo-cell areas smaller than 42μm^2, we further decided to include all nuclei with pseudo-cell areas in the lower quartile to construct the region with maximum nuclear crowding. Then, to construct the region with maximum delay in nuclear divisions, we simply marked the areas of the embryo that contain the last ~20% of the nuclei that finished nuclear cycle 13. This percentage was decided empirically: it corresponds to a region of similar size as that corresponding to the crowded region above. Here the rationale is drawn from previous studies which indicate that the regulation of nuclear division cycles is coordinated at the scale of the entire embryo (Deneke et al. 2016), and given that all of the nuclei share the same cytoplasm, a local delay in nuclear cycles would create conflicts between the biochemical status of the cytoplasm and the cell cycle stage of the delayed nuclei. Further, we combined the crowded and delayed regions using the logical OR operator, to test combinatorial effects of the nuclear crowding and nuclear cycle asynchrony. Finally, we computed the fraction of mitotic failures in areas thus constructed.

In the analysis to *compare the distribution of nuclei alongside that of F-actin*, was rather similar to the pipeline to *reconstruct the nuclear distribution in the whole embryo*, except that we didn't have 2 half-embryos to fuse, essentially starting from segmentation of embryo volume. Here, instead of

using nuclear staining, we segmented embryo volume using the F-actin staining. Then the 3D distance map similarly allowed us to classify pixels into cortical-, subcortical-, or yolk-regions based on their distance from embryo surface. The pixels in these regions were then color coded and presented as sum projections in Figure S9.

Figure and table legends:

Figure 1: Embryonic lethality and the loss of nuclear due to mitotic failures in embryos exposed to elevated temperature.

(A, B) To assess developmental robustness, we exposed embryos to various temperature regimen and estimated the embryo lethality. (A) Schematic showing the temperature regimen in the embryo survival experiment, starting from the beginning of embryo collection. Here we have three conditions depending on exposure to normal or elevated temperature regimen in the 3-hour time windows as shown, normal-normal [NN], elevated-normal [EN], and normal-elevated [NE]. In all cases, the first time-window also includes 1 hour of embryo collection. The embryonic development beyond 6 hours continued at normal temperature. (B) The scatter plots show the distribution of percent lethality in embryos from various conditions, calculated based on the fraction of embryos that don't hatch into larvae. Each dot represents data from a sample with ≥26 embryos.

(C-E) Montages of snapshots from live embryos, expressing Histone-RFP, from late interphase 11 till late interphase 14, in embryos developing either at normal temperatures (C), or at elevated temperature showing mild (D), or severe (E) defect. The nuclei were labelled as a function of their distance from the embryo surface. Here, green indicates cortical, and magenta indicates sub-cortical nuclei that are lost. At elevated temperature, a lot more nuclei are expelled, and as a result, we can see large gaps between cortical (green) nuclei, often coinciding with expelled (magenta) nuclei, especially during early interphase-14.

(F-H) To assess the pairwise loss of nuclei, we counted mitotic failures that lead to such nuclear expulsions. (F) Montage of snapshots from live embryo, from late interphase 12 to late interphase 13, where Histone-RFP marks the distribution of nuclei, cortical nuclei are in green and subcortical (expelled) nuclei are in magenta. The pairwise loss of nuclei due to mitotic failure is exemplified in an embryo developing at elevated temperature. The arrowheads track the segregating daughter nuclei that will be expelled eventually, while arrows exemplify normal nuclei. Of note, this type of nuclear loss occurs at all temperatures, though at different a frequency. (G) Scatter plot showing the distribution of events of nuclear losses due to mitotic failure during interphase 14. (H) The schematic to illustrate the phenomenon of mitotic failures at elevated temperature.

Scale bars in C-E are 25 µm, in F is 5 µm. B and G show scatters with median, with whiskers showing 95% CI. In G, the hollow markers indicate embryos that have a blastoderm hole, with large hollow markers indicating a single large hole, and small hollow markers indicating either a single or multiple small holes. *, $p<0.05$; **, $p<0.01$; ***, $p<0.001$; ****, $p<0.0001$, non-significant comparisons are not shown.

Figure 2: Nuclear cycle asynchrony and nuclear crowding increases as a function of temperature during embryo development.

(A-C) To assess the asynchrony in nuclear cycles, we identified the phases of nuclear cycle along the AP axis. (A) Image shows the entire anterior-posterior extent of the field of view, from a live embryo developing at 29°C. Histone-RFP marks the nuclei, cortical nuclei are in green and subcortical

838 (expelled) nuclei are in magenta. Different regions of the embryo have nuclei in different stages of
839 nuclear division cycle, as indicated above the image. Arrows show the direction in which the wave of
840 nuclear division cycle will progress. Here, we have an anterior- and a posterior-wave which will meet
841 in the central region of the embryo. The anterior, central, and posterior 1/5th of the field of view are
842 indicated below the image, with the anterior 1/5th of the embryo containing nuclei that are more
843 advanced in division cycle, as compared to the posterior 1/5th, which are yet more advanced than
844 the central 1/5th. As a result, these regions will enter the subsequent interphase in an asynchronous
845 manner (see also Figure S7). (B) Scatter plots showing the distribution of asynchrony for embryos at
846 various temperatures. (C) The schematic illustrates the progressive increase in asynchrony at
847 elevated temperature.

848 (D-Q) To assess the crowding of nuclei, we segmented the nuclei and generated pseudo-cells. The
849 figure shows data from of live embryos that were developing either at 22°C (D, H, L), 25°C (E, I, M),
850 28°C (F, J, N), or at 29°C (G, K, O). (D-G) Snapshots from live embryos at the end of interphase 13,
851 where Histone-RFP marks the nuclei. The outline shows the region of the image that is considered
852 for quantifications. (H-K) The pseudo-cells for the corresponding embryos in D-G. A pseudo cell is
853 centred on a nucleus, while the region of a pseudo-cell is bound by line segments that are
854 equidistant from neighbouring nuclei. Various pseudo-cells are colour-coded according to their area
855 in μm^2 according to the LUT at the bottom. (L-O) Plots showing the distribution of pseudo-cell areas
856 as a function of their anterior-posterior position, along with a quadratic fit through the distribution,
857 for embryos in D-G. (P) Scatter plots showing distribution of the coefficient of the quadratic term for
858 embryos at various temperatures. This essentially captures the extent of nuclear crowding, with
859 larger quadratic coefficient indicating greater crowding. (Q) The schematic illustrates the crowding
860 effect at elevated temperature. The size of the black arrows indicates the gradation in nuclear
861 density, from poles to the central region.

862 Scale bars, 20 µm. B and P shows scatters with median, with whiskers showing 95% CI. In B and P,
863 hollow markers indicate data from embryos that have blastoderm hole, with large hollow markers
864 indicating a single large hole, and small hollow markers indicating either a single or multiple small
865 holes. *, $p<0.05$; **, $p<0.01$; ***, $p<0.001$; non-significant comparisons are not shown.

866 **Figure 3: Nuclear crowding and nuclear cycle asynchrony combinatorially enhance mitotic failure**
867 **defect.**
868 (A, B) Snapshots from live embryo, developing at 29°C, at the end of interphase 13 (A), and 14 min
869 afterwards (B), where Histone-RFP marks the nuclei. The outline in A shows the region of the image
870 that is has nuclear crowding, while that in B bounds the region containing most delayed nuclei, i.e.,
871 those that are most lagging in nuclear division cycles. (C-E) The locations of lost pairs of nuclei during
872 interphase 14 are marked as white dots to indicate their distribution in the field of view. Then,
873 various regions are defined in the embryo to illustrate the fraction of mitotic failures occurring in
874 that region. These regions are composed based on, the crowded region only (C), the delayed region
875 only (D), and the combination of the crowded and delayed regions (E). (F-H) Scatter plots showing
876 the distribution of the area fractions in crowded (F), delayed (G), and crowded OR delayed (H)
877 regions of the embryos. In case of both crowded (F) and delayed (G) regions, the medians are rather
878 comparable across temperature, and the low variability within a given temperature is exaggerating
879 the differences across temperatures. In case of the area fraction of the 'crowded OR delayed'
880 regions (H), the increase in the overlap of crowded and delayed region reduces the overall size of the
881 combined region. (I-K) Plots showing the distribution of fraction of mitotic failures occurring in the

882 crowded region only (I), in the delayed region only (J), and in the combination of the crowded and
883 delayed regions (K).

884 Scale bars, 20 µm. F-K show scatters with median, with whiskers showing 95% CI. Hollow markers
885 indicate data from embryos that have blastoderm hole, with large hollow markers indicating a single
886 large hole, and small hollow markers indicating either a single or multiple small holes. *, p<0.05; **,
887 p<0.01; ***, p<0.001; non-significant comparisons are not shown.

888 **Figure 4: Rescue of embryonic lethality at elevated temperature through over-expression of the**
889 **regulators of cell polarity signalling or those of F-actin -microtubules interaction during mitosis,**
890 **and genes varying along thermoclines as "natural" candidates.**
891 (A) Scatter plot showing the distribution of percent lethality in embryos from various genotypes, at
892 normal (25°C) vs elevated temperature (29°C), calculated based on the fraction of embryos that
893 don't hatch into larvae. Each dot represents data from a sample with ≥12 embryos. (B, C) Scatter
894 plots showing the distribution of the fraction of mitotic failures in crowded regions (B), and in
895 crowded OR delayed regions (C), in the embryos at normal (22°C) vs elevated temperature (29°C).
896 Each dot represents data from one embryo. Additional quantifications related to this experiment are
897 presented in Figure S8.

898 (D) Scatter plots showing the distribution of percent lethality in embryos from various genotypes, at
899 normal (25°C) vs elevated temperature (29°C), calculated based on the fraction of embryos that
900 don't hatch into larvae. Each dot represents data from a sample with ≥18 embryos. (E, F) Scatter
901 plots showing the distribution of the fraction of mitotic failures in crowded regions (E), and in
902 crowded OR delayed regions (F), in the embryos at normal (22°C) vs elevated temperature (29°C).
903 Each dot represents data from one embryo. Additional quantifications related to this experiment are
904 presented in Figure S10.

905 (G) Pie charts showing the clinal distribution score for various genes associated with 'spindle
906 dynamics' (combination of GO terms, cell polarity, spindle organisation, and spindle localisation,
907 n=320 genes), or with GO term 'metabolic process' (n=6612 genes). ~40% of genes associated with
908 spindle dynamics, while ~30% of the genes associated with metabolic process, are clinal in at least
909 one continent.

910 A-F shows scatters with median, with whiskers showing 95% CI. In B, C, E, and F, hollow markers
911 indicate data from embryos that have blastoderm hole, with large hollow markers indicating a single
912 large hole, and small hollow markers indicating either a single or multiple small holes. *, p<0.05; **,
913 p<0.01; ***, p<0.001; ****, p<0.0001; non-significant comparisons are not shown.

914 **Figure S1: Blastoderm holes appear in a fraction of embryos at elevated temperature.**
915 The figure shows the snapshots from live embryos, expressing Histone-RFP, from early interphase
916 14, in embryos developed at elevated temperature. The nuclei are labelled as a function of their
917 distance from the embryo surface. Here, green indicates cortical, and magenta indicates sub-cortical
918 nuclei that are expelled, while arrows/arrowheads indicate large/small blastoderm holes. For
919 embryos with large blastoderm holes (embryo 05, and 08), we see many nuclei in magenta, while in
920 case of embryos with small blastoderm holes (embryos 04, and 09), we can see only a few nuclei in
921 magenta per hole. We would argue that development in *Drosophila* is robust enough to buffer the
922 defects due to the small holes, but fails at 29°C when large holes appear.

923 Scale bar, 25 µm.

924 **Figure S2: Nuclear loss shows left-right asymmetry in embryos developing at elevated**
925 **temperature.**
926 Distribution of nuclei in embryos during interphase 13, in fixed embryos that were developing either
927 at normal temperature (A, D, G, H), or at elevated temperature that show either a mild defect (B, E,
928 I, J) or a severe defect (C, F, K, L). (A-F) Maximum projections of the right and left halves of embryos,
929 where the nuclei are labelled as a function of their distance from the embryo surface. Here, green
930 indicates cortical nuclei, i.e., nuclei close to embryo surface, while magenta indicates sub-cortical
931 nuclei, i.e., nuclei that are deeper in the embryo, farther from embryo surface. The yolk nuclei are
932 not shown for improved visibility. As compared to embryos at normal temperature (A), those at
933 elevated temperature show mildly (B) or severely (C) numerous gaps in the distribution of cortical
934 nuclei. These gaps often also correspond to the locations of subcortical nuclei (A-C). Of note, the
935 embryo surface prediction gets distorted at the posterior pole, due to the pole cell nuclei that are
936 outside the embryo cortex, thus mislabelling cortical nuclei in magenta. These mis-coloured nuclei
937 were manually erased to exclusively highlight the subcortical nuclei (D-F). (G-L) Cross-sectional view
938 along the indicated regions in panels A-C. Here, yolk nuclei are additionally marked in yellow. The
939 arrow indicates the direction along which we can follow the surface of the embryo along the cross-
940 section. The cross-sections are chosen to specifically highlight the locations of subcortical nuclei.

941 Scale bars in A-C are 50 µm, while in G, I, and K are 25 µm.

942 **Figure S3: Out-of-plane nuclear divisions during mitosis 10, and the low frequency of isolated**
943 **nuclear expulsion during interphase 14, does not vary significantly with temperature, and cannot**
944 **explain the observed loss of nuclei.**
945 (A, B) Montages exemplifying out-of-plane division during mitosis 10 in an embryo developing at
946 25°C. Histone-RFP marks the nuclei (green), while Jupiter-GFP marks the microtubules (magenta).
947 Arrowheads exemplify in-plane divisions, while arrows exemplify out-of-plane division. Each
948 subsequent frame is 1min apart. In the x-y view of the divisions (A), only one of the daughter nuclei
949 is clearly visible after the out-of-plane division, while the other daughter nucleus is better seen in the
950 y-z view of the division (B), where we can see it translocating to the embryo interior. (C) Plots show
951 the number of out-of-plane divisions, that are visible in the field of view, in embryos developing at
952 various temperatures. For context, an embryo contains on the order of 70 mitotic spindles the field
953 of view at interphase 10. So, even though the p-value is <0.05 for the comparison between 22°C and
954 29°C, and given that there is no correlation between the number of out-of-plane divisions and the
955 presence of blastoderm holes, we would argue that the difference is not biologically significant.

956 (D) Montage exemplifying isolated nuclear expulsion in an embryo developing at 25°C, from
957 telophase 12 to late interphase 13. Histone-RFP marks the distribution of nuclei, cortical nuclei are in
958 green and subcortical (expelled) nuclei are in magenta. The arrowheads track the daughter nucleus
959 that will be expelled, while arrows track the daughter nucleus that will be retained cortically. (E)
960 Scatter plots showing the distribution of isolated loss of nuclei during interphase 14.

961 Scale bar in A is 10 µm, and in D is 5 µm. C and E show scatters with median, with whiskers showing
962 95% CI. The hollow markers indicate embryos that have a blastoderm hole, with large hollow
963 markers indicating a single large hole, and small hollow markers indicating either a single or multiple
964 small holes. *, p<0.05; non-significant comparisons are not shown.

965 **Figure S4: Defective nuclei take different amount of time to be expelled from embryo cortex.**
966 (A, B) The figure shows the montages of snapshots from live embryos, with a few representative

967 nuclei tracked from late interphase 12 to interphase 13. Top panels show Histone-RFP signal, while
968 bottom panels show Jupiter-GFP signal. Nuclei tagged in green/ magenta are the ones that arise
969 from mitotic defects during mitosis 10/ 11. All of these are expelled during interphase 13. Notice the
970 lack of spindle formation around the tagged nuclei. Also note that the nuclei expelled by the 5th
971 timepoint are not shown in the 6th timepoint. (A) An embryo developing at normal temperature,
972 where 1 magenta and 1 green nuclei are followed. (B) An embryo developing at elevated
973 temperature, where 6 magenta and 3 green nuclei are followed.

974 Scale bars are 20 µm. The numbers in inset indicate time in min:sec.

975 **Figure S5: Nuclear movement parallel to the embryo surface is amplified at elevated temperature.**
976 (A-C) An example depicting how nuclear movements, and the deviations thereof, are calculated.
977 Snapshots from live embryo developing at elevated temperature, where Histone-RFP marks the
978 distribution of nuclei, showing the mother nuclei at the end of interphase 10 (A) and the
979 corresponding 8 great-granddaughter nuclei, each, at the end of interphase 13 (C). The neighbouring
980 nuclear clusters are marked in either cyan or yellow. The trajectories of the center of nuclear
981 clusters (B) also indicate the increase in the number of nuclei due to divisions, as the broadening of
982 the tracks. The dotted lines indicate straight-lines fitted to individual trajectories, which are used as
983 reference for computing deviations for each time point of that trajectory. The shaded region
984 captures periods of greatest movement that starts with anaphase (see methods). (D, E) To quantify
985 the drift in the center of nuclear clusters, we compute the slope of the straight-line fits (dotted lines
986 in B). The median of slopes for all nuclear cluster from one embryo provides a robust estimate of the
987 drift in the centers of the nuclear clusters. Plots showing the distribution of these medians (one dot
988 per embryo), for the drift along AP axis (D), and for that along DV axis (E). (F-I) To quantify the
989 movements in the center of nuclear clusters during periods of maximum movement (shaded region
990 in B) and normal movement (unshaded regions in B), we compute the average of the deviations from
991 the straight-line fits (dotted lines in B). The median of such average deviations for all nuclear cluster
992 from one embryo provides a robust estimate of the nuclear cluster deviation. Plots showing the
993 distribution of these medians (one dot per embryo), for the fluctuations along AP axis (F, H), and for
994 those along DV axis (G, I), during interphase-metaphase (F, G) or during anaphase-telophase (H, I).

995 Scale bar is 25 µm. D to I show scatters with median, with whiskers showing 95% CI. Hollow markers
996 indicate data from embryos that have blastoderm hole, with large hollow markers indicating a single
997 large hole, and small hollow markers indicating either a single or multiple small holes. *, $p<0.05$; **,
998 $p<0.01$; ***, $p<0.001$; non-significant comparisons are not shown.

999 **Figure S6: Nuclear movement along surface-yolk axis is amplified at elevated temperature.**
1000 Cross-sections from live embryos, expressing Histone-RFP, from late interphase 13 till early
1001 interphase 14, in embryos developing either at normal temperature (A), or at elevated temperature
1002 (B). Here, the coloured lines mark the basal tip of nuclei in the first frames (t=-7:30 min) of the
1003 respective montage. Timepoint 00:00 corresponds to initiation of anaphase at the left/right extreme
1004 of the images, which is also the first time we see the shift from baseline.

1005 Arrowheads point out the local peak of the nuclear shift from the baseline, while arrow points
1006 expelled nuclei. As we can see, at elevated temperature, the nuclei shift significantly from the
1007 baseline, before returning to normal localisation by the time the nuclei enter the subsequent
1008 interphase. Also, the shift from baseline occurs progressively from anterior/posterior poles towards
1009 the central region.

1010 Scale bars are 25 µm. Cross-sections are in the lateral region of the embryos, anterior to the left.

1011 **Figure S7: Nuclear cycle asynchrony increases as a function of the temperature during embryo**
1012 **development.**
1013 (A, B) Montages of snapshots from metaphase 13 to early interphase 14, from live embryos
1014 developing either at 25°C (A), or at 29°C (B). Histone-RFP marks the nuclei, cortical nuclei are in
1015 green and subcortical (expelled) nuclei are in magenta. The dotted lines divide the field of view in 5
1016 equal parts. Numbers in the inset represent time in min:sec, while 00:00 is when anterior 1/5th of the
1017 embryo enters interphase 14. Boxes highlight entry into interphase 14 in that region. The black
1018 arrows indicate the time point of maximum synchrony, i.e., halfway between the anterior and
1019 posterior 1/5th of the embryo, when the nuclei in the central region should have entered interphase
1020 14. This point serves as the reference to estimate asynchrony (see methods).

1021 Scale bars, 25 µm.

1022 **Figure S8: Additional quantifications related to *baz* or *dlg* over-expression.**
1023 (A-F) The distribution of the pseudo-cell areas in embryos at the end of interphase 13, in live
1024 embryos developing either at normal temperatures (A, C, and E), or at elevated temperature (B, D,
1025 and F). The pseudo-cell areas in embryos of control genotype (A, B), in embryos over-expressing *baz*
1026 (C, D), or in embryos over-expressing *dlg* (E, F), are shown. Anterior is to the left, dorsal up. The LUT
1027 bar at the bottom indicates the colour code corresponding to the area of pseudo-cells. (G-K) Scatter
1028 plots showing the distribution of the area fractions in crowded (G), and crowded OR delayed (H)
1029 regions of the embryos, the distribution of the extent of nuclear crowding (I), the distribution of the
1030 nuclear cycle asynchrony (J), and the number of pairwise nuclear expulsions (i.e., the number of
1031 mitotic failures) during interphase 14 (K) for embryos from various genotypes, at normal (22°C) vs
1032 elevated temperature (29°C). Each dot represents data from one embryo.

1033 Scale bar, 25 µm. G-K show scatters with median, with whiskers showing 95% CI. Hollow markers
1034 indicate data from embryos that have blastoderm hole, with large hollow markers indicating a single
1035 large hole, and small hollow markers indicating either a single or multiple small holes. *, $p<0.05$; **,
1036 $p<0.01$; ***, $p<0.001$; non-significant differences are omitted.

1037 **Figure S9: Elevated temperature disrupts the association between nuclei and F-actin caps.**
1038 Distribution of nuclei and F-actin in embryos during interphase 13, in fixed embryos that were
1039 developing either at normal temperatures (A, C, D), or at elevated temperature (B, E, F). (A, B) The
1040 images show SUM projections of the DAPI stained nuclei (top image) and Phallacidin stained F-actin
1041 (bottom image) of representative embryos. In the top images, the nuclei are labelled as a function of
1042 their distance from the embryo surface, where green indicates cortical, and magenta indicates sub-
1043 cortical nuclei. The yolk nuclei are not shown. Anterior is on the left, dorsal up. (C-F) The top and
1044 bottom images show a zoomed-in view of the indicated regions in panels A and B. Here, arrowheads
1045 indicate the expelled nuclei (C, E top panels) and the structures of F-actin corresponding to them (C,
1046 E bottom panels), which should otherwise be localised around cortical nuclei. Then, the arrows
1047 indicate gaps between neighbouring nuclei (D, F top panels), which should normally be devoid of any
1048 F-actin structures (D, bottom panel), but contain small "actin caps" in embryos at elevated
1049 temperature (F, bottom panel).

1050 Scale bars, 25µm. The boxed regions are 60x60 µm.

1051 **Figure S10: Additional quantifications related to *αCat* or *sgg* over-expression.**
1052 (A-F) The distribution of the pseudo-cell areas in embryos at the end of interphase 13, in live
1053 embryos developing either at normal temperatures (A, C, and E), or at elevated temperature (B, D,
1054 and F). The pseudo-cell areas in embryos of control genotype (A, B), in embryos over-expressing
1055 *αCat* (C, D), or in embryos over-expressing *sgg* (E, F), are shown. Anterior is to the left, dorsal up. The
1056 LUT bar at the bottom indicates the colour code corresponding to the area of pseudo-cells. (G-K)
1057 Scatter plots showing the distribution of the area fractions in crowded (G), and crowded OR delayed
1058 (H) regions of the embryos, the distribution of the extent of nuclear crowding (I), the distribution of
1059 the nuclear cycle asynchrony (J), and the number of pairwise nuclear expulsions (i.e., the number of
1060 mitotic failures) during interphase 14 (K) for embryos from various genotypes, at normal (22°C) vs
1061 elevated temperature (29°C). Each dot represents data from one embryo.

1062 Scale bar, 25 µm. G-K show scatters with median, with whiskers showing 95% CI. Hollow markers
1063 indicate data from embryos that have blastoderm hole, with large hollow markers indicating a single
1064 large hole, and small hollow markers indicating either a single or multiple small holes. *, $p<0.05$; **,
1065 $p<0.01$; ***, $p<0.001$; non-significant differences are omitted.

1066 **Figure S11: *mud* or *insc* over-expression does not ameliorate embryo survival at elevated**
1067 **temperature.**
1068 Scatter plot shows the distribution of percent lethality in embryos from various genotypes, at normal
1069 (25°C) vs elevated temperature (29°C), calculated based on the fraction of embryos that don't hatch
1070 into larvae. Each dot represents data from a sample with ≥21 embryos. As we can see in the plot,
1071 neither *mud* nor *insc* over-expression rescues the embryo lethality at elevated temperature, with
1072 *mud* over-expression increasing embryo lethality even at normal temperature (25°C).

1073 The plot shows scatters with median, while whiskers showing 95% CI. *, $p<0.05$; **, $p<0.01$; ***,
1074 $p<0.001$; non-significant differences are omitted.

1075 **Table S1:** This table contains genes that are identified as being clinal in different continents. Columns
1076 A to C contains lists of studies, and under the studies is a list of genes that are identified in these
1077 studies as being clinal. Column A, B, and C respectively list studies that have data from the
1078 continents of Australia and/or Australasia (AUS), North and/or Central America (USA), and Europe
1079 and/or North Africa (EU).

1080 We collect all the genes associated with the GO terms 'cell polarity', 'spindle organization', and
1081 'spindle localization', to compile a non-redundant master list of candidate genes associated with
1082 'spindle dynamics' in Column F. For each gene in column F, we count the number of times the gene
1083 appears in column A to C, counting a maximum of once per column, to respectively populate
1084 columns G to I. For each gene in column F, column J contains the sum of values in G, H, and I, to
1085 indicate the number of continents in which a gene is clinal. Each gene gets a score from 1 to 3, and
1086 we consider the gene to be a relevant candidate if it is found in at least 2 columns.

1087 We collect all the genes associated with the GO term 'metabolic process', to compile a control list of
1088 candidate genes in Column L. For each gene in column L, we count the number of times the gene
1089 appears in column A to C, counting a maximum of once per column, to respectively populate
1090 columns M to O. For each gene in column L, column P contains the sum of values in M, N, and O, to
1091 indicate the number of continents in which a gene is clinal. Thus, each gene gets a score from 1 to 3.

Following articles were used to source the list of genes in column A (Oakeshott, McKechnie, and Chambers 1984; McColl and McKechnie 1999; Bettencourt et al. 2002; Frydenberg, Hoffmann, and Loeschcke 2003; Umina et al. 2005; Sawyer et al. 2006; Weeks, Mckechnie, and Hoffmann 2006; Rand et al. 2010; Kolaczkowski et al. 2011; Paaby et al. 2014), column B (Vigue and Johnson 1973; Oakeshott, McKechnie, and Chambers 1984; Berry and Kreitman 1993; Duvernell and Eanes 2000; P. S. Schmidt, Duvernell, and Eanes 2000; Verrelli and Eanes 2001; Duvernell, Schmidt, and Eanes 2003; Sezgin et al. 2004; P. S. Schmidt and Paaby 2008; Rand et al. 2010; Fabian et al. 2012; Paaby et al. 2014; Machado et al. 2016), and column C (Oakeshott, McKechnie, and Chambers 1984; Costa et al. 1992; Weeks, Mckechnie, and Hoffmann 2006; Kapun et al. 2020).

Table S2: Column A lists candidates from Table S1 column F that have a score of 2 or higher, i.e., those that show selectable variation in natural populations. For these genes, we query FlyBase (http://flybase.org/batchdownload) for additional details like, gene name (column B), gene symbol (column C), and the level of expression for these genes during the first 2 hours of embryo development (column D). The level of expression is based on published transcriptomics data (Graveley et al. 2011), which would correspond to maternal pool of mRNAs, and the most relevant developmental window for this study. The candidate genes clinal in all 3 continents are highlighted in green.

Columns F-J present a table with counts of genes that are associated with various categories of genes in Table S1 column F and L, and a further breakdown of how many of these genes are clinal in how many continents. The breackdown is also plotted as pie-charts in Figure 4G.

Table S3: This table lists various figure panels (columns A and B), and the related parental genotypes, i.e., the genotypes of females (column C) and males (column D) present in the embryo collection cages for the experiment related to a figure panel.

Additional information

Data and Code Availability:
Data and codes developed for data analysis are available upon request from corresponding authors.

Author contributions:
G.K. and S.L. planned the project. G.K. did the experiments with help from P.A. for baz and dlg overexpressions, and JJ.D.-L. for embryo fixation, and nuclei and F-actin staining. G.K. did the image analyses and statistical analyses. G.K. and S.L. wrote the manuscript, and all authors gave comments on the manuscript.

Acknowledgments:
We would like to thank Lazero Centanin, Nicolas Gompel, and Marianthi Karageorgi for insightful comments on various drafts of the manuscript. We are grateful to Jochen Wittbrodt for his enthusiasm, and for his continuous and generous support. We would also like to thank Ingrid Lohmann for *Drosophila* culture related support, and Thomas Lecuit for sharing fly lines. This work wass funded by the DFG (LE 2787/3-1) to S.L., while G.K. was supported through an HFSP Long-term postdoctoral fellowship (LT000597/2019-L).

Competing interests:
The authors declare no competing financial interest.

References:

1133 Berry, A., and M. Kreitman. 1993. “Molecular Analysis of an Allozyme Cline: Alcohol Dehydrogenase
1134 in Drosophila Melanogaster on the East Coast of North America.” *Genetics* 134 (3): 869–93.
1135 https://doi.org/10.1093/genetics/134.3.869.

1136 Bettencourt, Brian R., Inyoung Kim, A. A. Hoffmann, and M. E. Feder. 2002. “Response to Natural and
1137 Laboratory Selection at the Drosophila Hsp70 Genes.” *Evolution* 56 (9): 1796–1801.
1138 https://doi.org/10.1111/j.0014-3820.2002.tb00193.x.

1139 Bogovic, John A., Philipp Hanslovsky, Allan Wong, and Stephan Saalfeld. 2016. “Robust Registration
1140 of Calcium Images by Learned Contrast Synthesis.” In *2016 IEEE 13th International Symposium*
1141 *on Biomedical Imaging (ISBI)*, 2016-June:1123–26. IEEE.
1142 https://doi.org/10.1109/ISBI.2016.7493463.

1143 Cao, Jian, Justin Crest, Barbara Fasulo, and William Sullivan. 2010. “Cortical Actin Dynamics Facilitate
1144 Early-Stage Centrosome Separation.” *Current Biology : CB* 20 (8): 770–76.
1145 https://doi.org/10.1016/j.cub.2010.02.060.

1146 Chong, Jeronica, Christopher Amourda, and Timothy E. Saunders. 2018. “Temporal Development of
1147 Drosophila Embryos Is Highly Robust across a Wide Temperature Range.” *Interface* 15 (144).
1148 https://doi.org/10.1098/rsif.2018.0304.

1149 Costa, Rodolfo, Alexandre A. Peixoto, Guido Barbujani, and Charalambos P. Kyriacou. 1992. “A
1150 Latitudinal Cline in a Drosophila Clock Gene.” *Proceedings of Royal Society of London*, 43–49.

1151 Crews, Sarah M., W Tyler McCleery, and M. Shane Hutson. 2016. “Pathway to a Phenocopy: Heat
1152 Stress Effects in Early Embryogenesis.” *Developmental Dynamics : An Official Publication of the*
1153 *American Association of Anatomists* 245 (3): 402–13. https://doi.org/10.1002/dvdy.24360.

1154 Deneke, Victoria E., Anna Melbinger, Massimo Vergassola, and Stefano Di Talia. 2016. “Waves of
1155 Cdk1 Activity in S Phase Synchronize the Cell Cycle in Drosophila Embryos.” *Developmental Cell*
1156 38 (4): 399–412. https://doi.org/10.1016/j.devcel.2016.07.023.

1157 Duvernell, David D., and W. F. Eanes. 2000. “Contrasting Molecular Population Genetics of Four
1158 Hexokinases in Drosophila Melanogaster, D. Simulans and D. Yakuba.” *Genetics* 156 (3): 1191–
1159 1201. https://doi.org/10.1093/genetics/156.3.1191.

1160 Duvernell, David D., Paul S. Schmidt, and Walter F. Eanes. 2003. “Clines and Adaptive Evolution in
1161 the Methuselah Gene Region in Drosophila Melanogaster.” *Molecular Ecology* 12 (5): 1277–85.
1162 https://doi.org/10.1046/j.1365-294X.2003.01841.x.

1163 Edwards, Marshall J. 2006. “Review: Hyperthermia and Fever during Pregnancy.” *Birth Defects*
1164 *Research. Part A, Clinical and Molecular Teratology* 76 (7): 507–16.
1165 https://doi.org/10.1002/bdra.20277.

1166 Fabian, Daniel K., Martin Kapun, Viola Nolte, Robert Kofler, Paul S. Schmidt, Christian Schlötterer,
1167 and Thomas Flatt. 2012. “Genome-Wide Patterns of Latitudinal Differentiation among
1168 Populations of Drosophila Melanogaster from North America.” *Molecular Ecology* 21 (19):
1169 4748–69. https://doi.org/10.1111/j.1365-294X.2012.05731.x.

1170 Figard, Lauren, Liuliu Zheng, Natalie Biel, Zenghui Xue, Hasan Seede, Seth Coleman, Ido Golding, and
1171 Anna Marie Sokac. 2019. “Cofilin-Mediated Actin Stress Response Is Maladaptive in Heat-
1172 Stressed Embryos.” *Cell Reports* 26 (13): 3493-3501.e4.
1173 https://doi.org/10.1016/j.celrep.2019.02.092.

1174 Foe, V. E., and B. M. Alberts. 1983. “Studies of Nuclear and Cytoplasmic Behaviour during the Five
1175 Mitotic Cycles That Precede Gastrulation in Drosophila Embryogenesis.” *Journal of Cell Science*
1176 61 (May): 31–70. https://doi.org/10.1242/jcs.61.1.31.

1177 Foe, V.E. 1989. “Mitotic Domains Reveal Early Commitment of Cells in Drosophila Embryos.” *Trends*

1178 *in Genetics* 5 (C): 322. https://doi.org/10.1016/0168-9525(89)90120-0.

1179 Frydenberg, Jane, A. A. Hoffmann, and Volker Loeschcke. 2003. "DNA Sequence Variation and
1180 Latitudinal Associations in Hsp23, Hsp26 and Hsp27 from Natural Populations of Drosophila
1181 Melanogaster." *Molecular Ecology* 12 (8): 2025–32. https://doi.org/10.1046/j.1365-
1182 294X.2002.01882.x.

1183 Graham, John M. 2020. "Update on the Gestational Effects of Maternal Hyperthermia." *Birth Defects*
1184 *Research* 112 (12): 943–52. https://doi.org/10.1002/bdr2.1696.

1185 Graveley, Brenton R., Angela N. Brooks, Joseph W. Carlson, Michael O. Duff, Jane M. Landolin, Li
1186 Yang, Carlo G. Artieri, et al. 2011. "The Developmental Transcriptome of Drosophila
1187 Melanogaster." *Nature* 471 (7339): 473–79. https://doi.org/10.1038/nature09715.

1188 Graziosi, G., F. Micali, R. Marzari, F. de Cristini, and A. Savoini. 1980. "Variability of Response of
1189 EarlyDrosophila Embryos to Heat Shock." *Journal of Experimental Zoology* 214 (2): 141–45.
1190 https://doi.org/10.1002/jez.1402140203.

1191 Harris, Tony J C, and Mark Peifer. 2004. "Adherens Junction-Dependent and -Independent Steps in
1192 the Establishment of Epithelial Cell Polarity in Drosophila." *The Journal of Cell Biology* 167 (1):
1193 135–47. https://doi.org/10.1083/jcb.200406024.

1194 Herbert, Sébastien, Léo Valon, Laure Mancini, Nicolas Dray, Paolo Caldarelli, Jérôme Gros, Elric
1195 Esposito, et al. 2021. "LocalZProjector and DeProj: A Toolbox for Local 2D Projection and
1196 Accurate Morphometrics of Large 3D Microscopy Images." *BMC Biology* 19 (1): 136.
1197 https://doi.org/10.1186/s12915-021-01037-w.

1198 IPBES. 2019. *The Global Assessment Report of the Intergovernmental Science-Policy Platform on*
1199 *Biodiversity and Ecosystem Services*. https://doi.org/10.5281/zenodo.3831673.

1200 Kapun, Martin, Maite G Barrón, Fabian Staubach, Darren J. Obbard, R Axel W Wiberg, Jorge Vieira,
1201 Clément Goubert, et al. 2020. "Genomic Analysis of European Drosophila Melanogaster
1202 Populations Reveals Longitudinal Structure, Continent-Wide Selection, and Previously
1203 Unknown DNA Viruses." *Molecular Biology and Evolution* 37 (9): 2661–78.
1204 https://doi.org/10.1093/molbev/msaa120.

1205 Khoury, Mark J., and David Bilder. 2020. "Distinct Activities of Scrib Module Proteins Organize
1206 Epithelial Polarity." *Proceedings of the National Academy of Sciences of the United States of*
1207 *America* 117 (21): 11531–40. https://doi.org/10.1073/pnas.1918462117.

1208 ———. 2022. "Minimal Functional Domains of the Core Polarity Regulator Dlg." *Biology Open* 11 (7).
1209 https://doi.org/10.1242/bio.059408.

1210 Kolaczkowski, Bryan, Andrew D. Kern, Alisha K. Holloway, and David J. Begun. 2011. "Genomic
1211 Differentiation between Temperate and Tropical Australian Populations of Drosophila
1212 Melanogaster." *Genetics* 187 (1): 245–60. https://doi.org/10.1534/genetics.110.123059.

1213 Kuntz, Steven G., and Michael B. Eisen. 2014. "Drosophila Embryogenesis Scales Uniformly across
1214 Temperature in Developmentally Diverse Species." *PLoS Genetics* 10 (4): e1004293.
1215 https://doi.org/10.1371/journal.pgen.1004293.

1216 ———. 2015. "Oxygen Changes Drive Non-Uniform Scaling in Drosophila Melanogaster
1217 Embryogenesis." *F1000Research* 4 (May): 1102.
1218 https://doi.org/10.12688/f1000research.7221.1.

1219 Lecuit, Thomas, and Alpha S. Yap. 2015. "E-Cadherin Junctions as Active Mechanical Integrators in
1220 Tissue Dynamics." *Nature Cell Biology* 17 (5): 533–39. https://doi.org/10.1038/ncb3136.

1221 Lemke, Steffen, Girish Kale, and Silvia Urbansky. 2020. "Comparing Gastrulation in Flies: Links
1222 between Cell Biology and the Evolution of Embryonic Morphogenesis." *Mechanisms of*

1223 *Development* 164 (October): 103648. https://doi.org/10.1016/j.mod.2020.103648.

1224 Lockwood, Brent L., Cole R. Julick, and Kristi L. Montooth. 2017. "Maternal Loading of a Small Heat
1225 Shock Protein Increases Embryo Thermal Tolerance in Drosophila Melanogaster." *The Journal*
1226 *of Experimental Biology* 220 (Pt 23): 4492–4501. https://doi.org/10.1242/jeb.164848.

1227 Lu, Xuemin, Jennifer M. Li, Olivier Elemento, Saeed Tavazoie, and Eric F. Wieschaus. 2009. "Coupling
1228 of Zygotic Transcription to Mitotic Control at the Drosophila Mid-Blastula Transition."
1229 *Development (Cambridge, England)* 136 (12): 2101–10. https://doi.org/10.1242/dev.034421.

1230 Lynch, Jeremy A., Ezzat El-Sherif, and Susan J. Brown. 2012. "Comparisons of the Embryonic
1231 Development of Drosophila , Nasonia , and Tribolium." *Wiley Interdisciplinary Reviews:*
1232 *Developmental Biology* 1 (1): 16–39. https://doi.org/10.1002/wdev.3.

1233 Machado, Heather E., Alan O. Bergland, Katherine R. O'Brien, Emily L. Behrman, Paul S. Schmidt, and
1234 Dmitri A. Petrov. 2016. "Comparative Population Genomics of Latitudinal Variation in
1235 Drosophila Simulans and Drosophila Melanogaster." *Molecular Ecology* 25 (3): 723–40.
1236 https://doi.org/10.1111/mec.13446.

1237 Mapelli, Marina, and Cayetano Gonzalez. 2012. "On the Inscrutable Role of Inscuteable: Structural
1238 Basis and Functional Implications for the Competitive Binding of NuMA and Inscuteable to
1239 LGN." *Open Biology* 2 (8): 120102. https://doi.org/10.1098/rsob.120102.

1240 Martin, Adam C. 2020. "The Physical Mechanisms of Drosophila Gastrulation: Mesoderm and
1241 Endoderm Invagination." *Genetics* 214 (3): 543–60.
1242 https://doi.org/10.1534/genetics.119.301292.

1243 Mazumdar, Aveek, and Manjari Mazumdar. 2002. "How One Becomes Many: Blastoderm
1244 Cellularization in Drosophila Melanogaster." *BioEssays : News and Reviews in Molecular,*
1245 *Cellular and Developmental Biology* 24 (11): 1012–22. https://doi.org/10.1002/bies.10184.

1246 McCartney, Brooke M., Donald G. McEwen, Elizabeth Grevengoed, Paul Maddox, Amy Bejsovec, and
1247 Mark Peifer. 2001. "Drosophila APC2 and Armadillo Participate in Tethering Mitotic Spindles to
1248 Cortical Actin." *Nature Cell Biology* 3 (10): 933–38. https://doi.org/10.1038/ncb1001-933.

1249 McColl, Gawain, and Stephen W. McKechnie. 1999. "The Drosophila Heat Shock Hsr-Omega Gene:
1250 An Allele Frequency Cline Detected by Quantitative PCR." *Molecular Biology and Evolution* 16
1251 (11): 1568–74. https://doi.org/10.1093/oxfordjournals.molbev.a026069.

1252 Miller, Morton W., and Charles C. Church. 2013. "Arrhenius Thermodynamics and Birth Defects:
1253 Chemical Teratogen Synergy. Untested, Testable, and Projected Relevance." *Birth Defects*
1254 *Research. Part C, Embryo Today : Reviews* 99 (1): 50–60. https://doi.org/10.1002/bdrc.21025.

1255 Oakeshott, J. G., S. W. McKechnie, and G. K. Chambers. 1984. "Population Genetics of the
1256 Metabolically Related Adh, Gpdh and Tpi Polymorphisms in Drosophila Melanogaster I.
1257 Geographic Variation in Gpdh and Tpi Allele Frequencies in Different Continents." *Genetica* 63
1258 (1): 21–29. https://doi.org/10.1007/BF00137461.

1259 Paaby, Annalise B., Alan O. Bergland, Emily L. Behrman, and Paul S. Schmidt. 2014. "A Highly
1260 Pleiotropic Amino Acid Polymorphism in the Drosophila Insulin Receptor Contributes to Life-
1261 History Adaptation." *Evolution; International Journal of Organic Evolution* 68 (12): 3395–3409.
1262 https://doi.org/10.1111/evo.12546.

1263 Pietzsch, Tobias, Stephan Saalfeld, Stephan Preibisch, and Pavel Tomancak. 2015. "BigDataViewer:
1264 Visualization and Processing for Large Image Data Sets." *Nature Methods* 12 (6): 481–83.
1265 https://doi.org/10.1038/nmeth.3392.

1266 Preibisch, Stephan, Stephan Saalfeld, and Pavel Tomancak. 2009. "Globally Optimal Stitching of Tiled
1267 3D Microscopic Image Acquisitions." *Bioinformatics (Oxford, England)* 25 (11): 1463–65.

https://doi.org/10.1093/bioinformatics/btp184.

Pritchard, David K., and Gerold Schubiger. 1996. “Activation of Transcription in Drosophila Embryos Is a Gradual Process Mediated by the Nucleocytoplasmic Ratio.” *Genes & Development* 10 (9): 1131–42. https://doi.org/10.1101/gad.10.9.1131.

Raguso, Robert A. 2020. “Don’t Forget the Flies: Dipteran Diversity and Its Consequences for Floral Ecology and Evolution.” *Applied Entomology and Zoology* 55 (1): 1–7. https://doi.org/10.1007/s13355-020-00668-9.

Rand, David M., Daniel M. Weinreich, Daniel Lerman, Donna Folk, and George W. Gilchrist. 2010. “Three Selections Are Better than One: Clinal Variation of Thermal QTL from Independent Selection Experiments in Drosophila.” *Evolution* 64 (10): 2921–34. https://doi.org/10.1111/j.1558-5646.2010.01039.x.

Rim, Ellen Youngsoo, Hans Clevers, and Roel Nusse. 2022. “The Wnt Pathway: From Signaling Mechanisms to Synthetic Modulators.” *Annual Review of Biochemistry* 91 (June): 571–98. https://doi.org/10.1146/annurev-biochem-040320-103615.

Rizzelli, Francesca, Maria Grazia Malabarba, Sara Sigismund, and Marina Mapelli. 2020. “The Crosstalk between Microtubules, Actin and Membranes Shapes Cell Division.” *Open Biology* 10 (3): 190314. https://doi.org/10.1098/rsob.190314.

Rudman, Seth M., Sharon I. Greenblum, Subhash Rajpurohit, Nicolas J. Betancourt, Jinjoo Hanna, Susanne Tilk, Tuya Yokoyama, Dmitri A. Petrov, and Paul S. Schmidt. 2022. “Direct Observation of Adaptive Tracking on Ecological Time Scales in Drosophila.” *Science (New York, N.Y.)* 375 (6586): eabj7484. https://doi.org/10.1126/science.abj7484.

Rutherford, Suzanne L., and Susan Lindquist. 1998. “Hsp90 as a Capacitor for Morphological Evolution.” *Nature* 396 (6709): 336–42. https://doi.org/10.1038/24550.

Sangster, Todd A., Susan Lindquist, and Christine Queitsch. 2004. “Under Cover: Causes, Effects and Implications of Hsp90-Mediated Genetic Capacitance.” *BioEssays : News and Reviews in Molecular, Cellular and Developmental Biology* 26 (4): 348–62. https://doi.org/10.1002/bies.20020.

Sawyer, Lesley A., Federica Sandrelli, Carlo Pasetto, Alexandre A. Peixoto, Ezio Rosato, Rodolfo Costa, and Charalambos P. Kyriacou. 2006. “The Period Gene Thr-Gly Polymorphism in Australian and African Drosophila Melanogaster Populations: Implications for Selection.” *Genetics* 174 (1): 465–80. https://doi.org/10.1534/genetics.106.058792.

Schmidt, Anja, and Jörg Grosshans. 2018. “Dynamics of Cortical Domains in Early Drosophila Development.” *Journal of Cell Science* 131 (7). https://doi.org/10.1242/jcs.212795.

Schmidt, Paul S., David D. Duvernell, and Walter F. Eanes. 2000. “Adaptive Evolution of a Candidate Gene for Aging in Drosophila.” *Proceedings of the National Academy of Sciences of the United States of America* 97 (20): 10861–65. https://doi.org/10.1073/pnas.190338897.

Schmidt, Paul S., and Annalise B. Paaby. 2008. “Reproductive Diapause and Life-History Clines in North American Populations of Drosophila Melanogaster.” *Evolution* 62 (5): 1204–15. https://doi.org/10.1111/j.1558-5646.2008.00351.x.

Sezgin, Efe, David D. Duvernell, Luciano M. Matzkin, Yihao Duan, Chen Tseh Zhu, Brian C. Verrelli, and Walter F. Eanes. 2004. “Single-Locus Latitudinal Clines and Their Relationship to Temperate Adaptation in Metabolic Genes and Derived Alleles in Drosophila Melanogaster.” *Genetics* 168 (2): 923–31. https://doi.org/10.1534/genetics.104.027649.

Telley, Ivo A., Imre Gáspár, Anne Ephrussi, and Thomas Surrey. 2012. “Aster Migration Determines the Length Scale of Nuclear Separation in the Drosophila Syncytial Embryo.” *The Journal of Cell*

Biology 197 (7): 887–95. https://doi.org/10.1083/jcb.201204019.

Umina, P. A., A. R. Weeks, M. R. Kearney, S. W. McKechnie, and A. A. Hoffmann. 2005. "Evolution: A Rapid Shift in a Classic Clinal Pattern in Drosophila Reflecting Climate Change." *Science* 308 (5722): 691–93. https://doi.org/10.1126/science.1109523.

Vazquez, Julio, Daniel Pauli, and Alfred Tissières. 1993. "Transcriptional Regulation in Drosophila during Heat Shock: A Nuclear Run-on Analysis." *Chromosoma* 102 (4): 233–48. https://doi.org/10.1007/BF00352397.

Verrelli, B. C., and W. F. Eanes. 2001. "Clinal Variation for Amino Acid Polymorphisms at the Pgm Locus in Drosophila Melanogaster." *Genetics* 157 (4): 1649–63. https://doi.org/10.1093/genetics/157.4.1649.

Vigue, C. L., and F. M. Johnson. 1973. "Isozyme Variability in Species of the Genus Drosophila. VI. Frequency-Property-Environment Relationships of Allelic Alcohol Dehydrogenases in D. Melanogaster." *Biochemical Genetics* 9 (3): 213–27.

Walter, Marika F., Nancy S. Petersen, and Harald Biessmann. 1990. "Heat Shock Causes the Collapse of the Intermediate Filament Cytoskeleton in Drosophila Embryos." *Developmental Genetics* 11 (4): 270–79. https://doi.org/10.1002/dvg.1020110405.

Weeks, A. R., S. W. Mckechnie, and A. A. Hoffmann. 2006. "In Search of Clinal Variation in the Period and Clock Timing Genes in Australian Drosophila Melanogaster Populations." *Journal of Evolutionary Biology* 19 (2): 551–57. https://doi.org/10.1111/j.1420-9101.2005.01013.x.

Welte, Michael A., Joan M. Tetrault, Robert P. Dellavalle, and Susan L. Lindquist. 1993. "A New Method for Manipulating Transgenes: Engineering Heat Tolerance in a Complex, Multicellular Organism." *Current Biology* 3 (12): 842–53. https://doi.org/10.1016/0960-9822(93)90218-D.

Xie, Yi, and J. Todd Blankenship. 2018. "Differentially-Dimensioned Furrow Formation by Zygotic Gene Expression and the MBT." *PLoS Genetics* 14 (1): e1007174. https://doi.org/10.1371/journal.pgen.1007174.

Zheng, Liuliu, Leonardo A. Sepúlveda, Rhonald C. Lua, Olivier Lichtarge, Ido Golding, and Anna Marie Sokac. 2013. "The Maternal-to-Zygotic Transition Targets Actin to Promote Robustness during Morphogenesis." *PLoS Genetics* 9 (11): e1003901. https://doi.org/10.1371/journal.pgen.1003901.

Figure 1

Increased embryonic lethality at elevated temperature

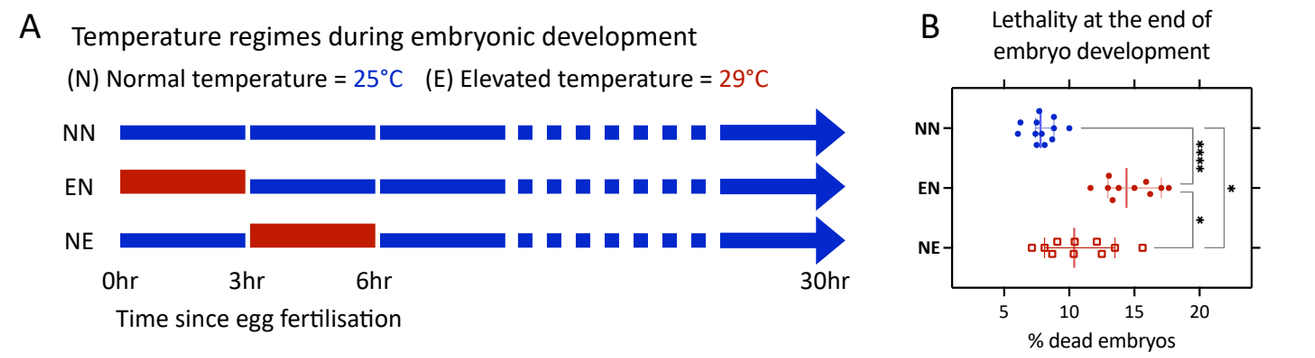

Nuclear loss phenotype at elevated temperature

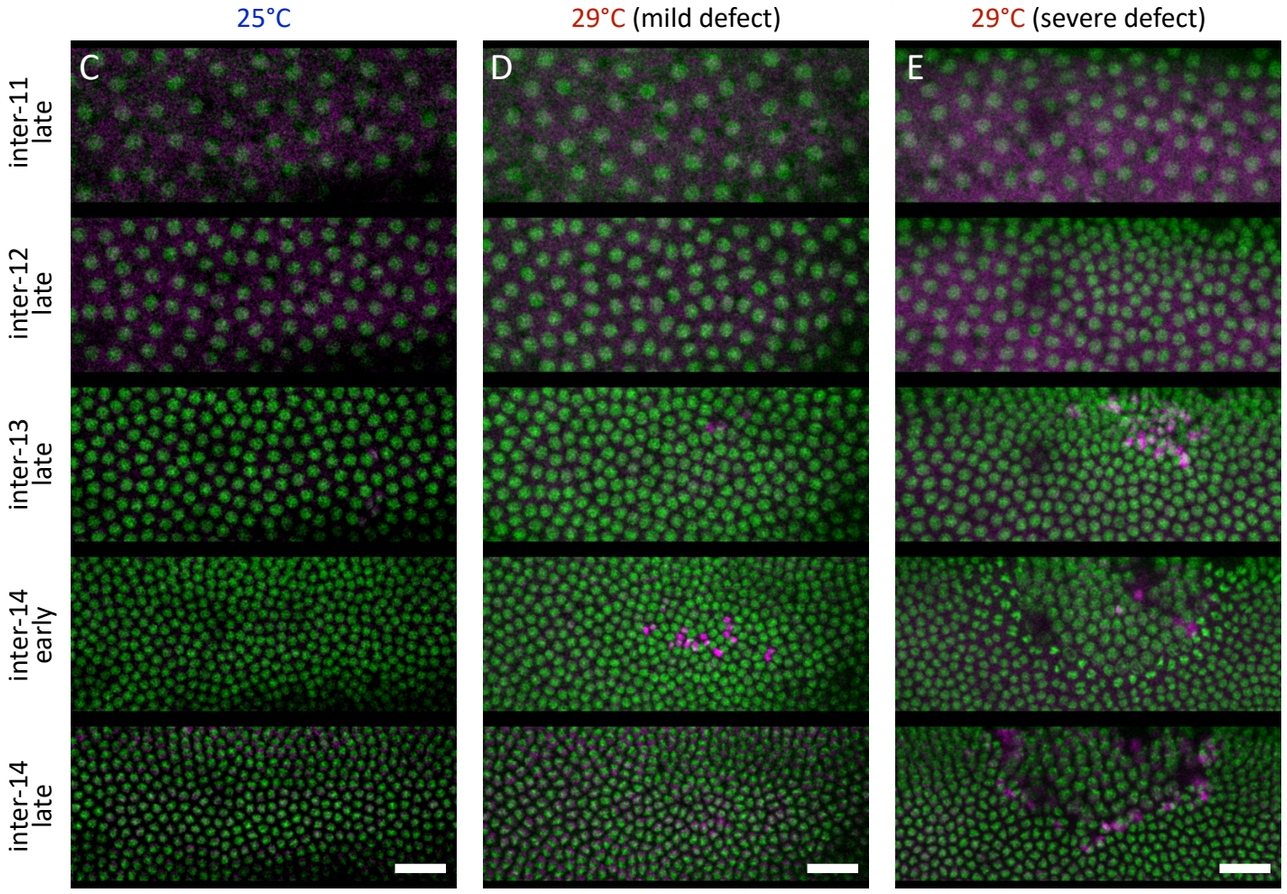

Mitotic failure and pairwise nuclear expulsion

(Example from embryo at 29°C)

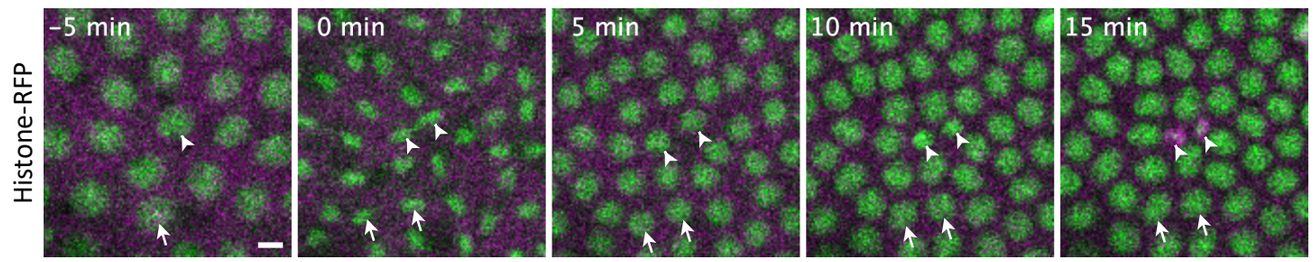

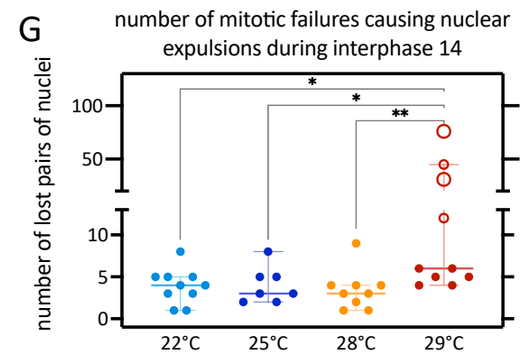

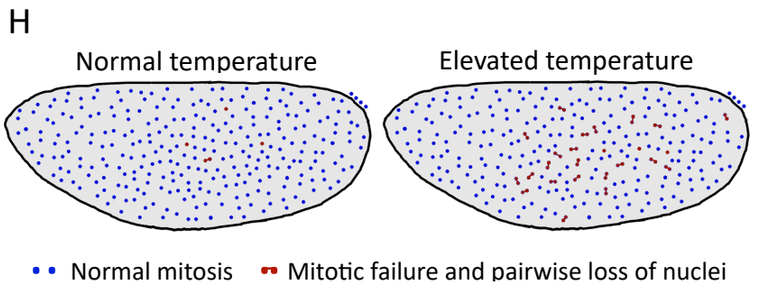

Figure 2

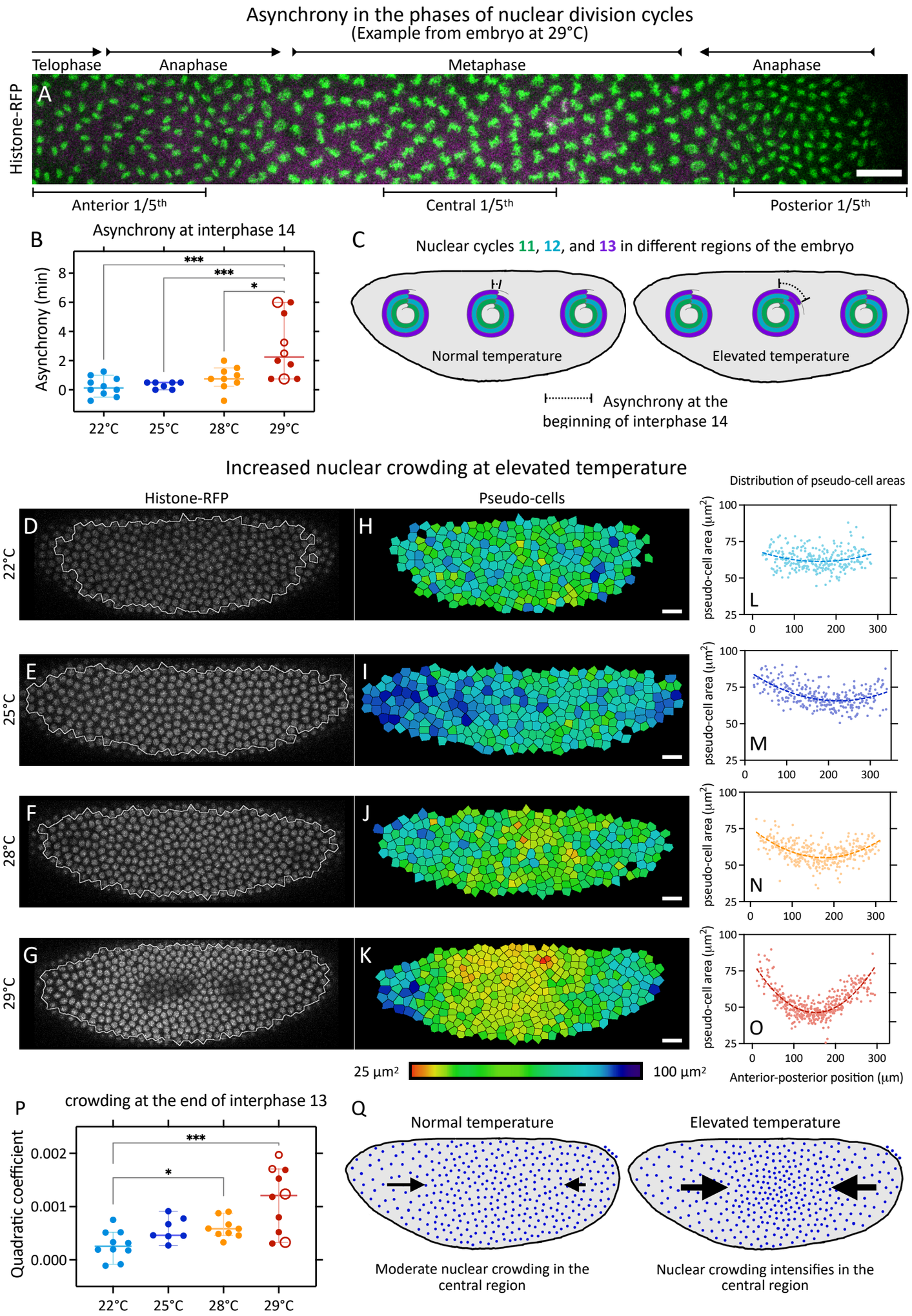
Asynchrony in the phases of nuclear division cycles
(Example from embryo at 29°C)
Telophase
Anaphase
Metaphase
Anaphase
Histone-RFP
A
Anterior 1/5th
Central 1/5th
Posterior 1/5th
B
Asynchrony at interphase 14
Asynchrony (min)
***
***
*
22°C
25°C
28°C
29°C
C
Nuclear cycles 11, 12, and 13 in different regions of the embryo
Normal temperature
Elevated temperature
Asynchrony at the beginning of interphase 14
Increased nuclear crowding at elevated temperature
Histone-RFP
Pseudo-cells
Distribution of pseudo-cell areas
22°C
25°C
28°C
29°C
D
E
F
G
H
I
J
K
L
M
N
O
pseudo-cell area (µm²)
Anterior-posterior position (µm)
25 µm²
100 µm²
P
crowding at the end of interphase 13
Quadratic coefficient
***
*
Q
Normal temperature
Elevated temperature
Moderate nuclear crowding in the central region
Nuclear crowding intensifies in the central region

Figure 3

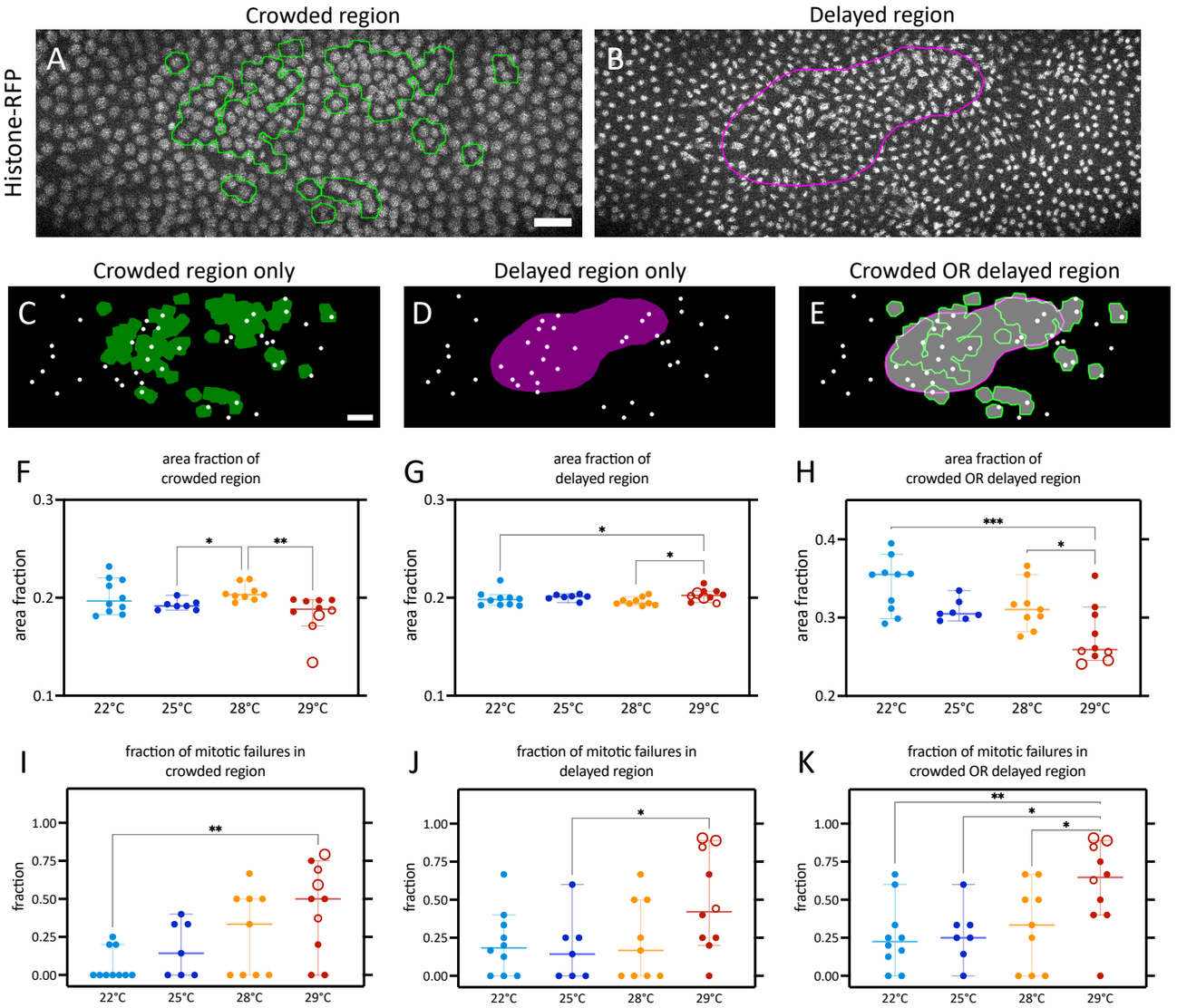
Crowded region
Delayed region
Histone-RFP
A
B
Crowded region only
Delayed region only
Crowded OR delayed region
C
D
E
F
area fraction of crowded region
area fraction
G
area fraction of delayed region
H
area fraction of crowded OR delayed region
I
fraction of mitotic failures in crowded region
fraction
J
fraction of mitotic failures in delayed region
K
fraction of mitotic failures in crowded OR delayed region
22°C
25°C
28°C
29°C

Figure 4

Over-expressing regulators of 'cell polarity signalling during mitosis'
to rescue embryonic lethality at elevated temperature

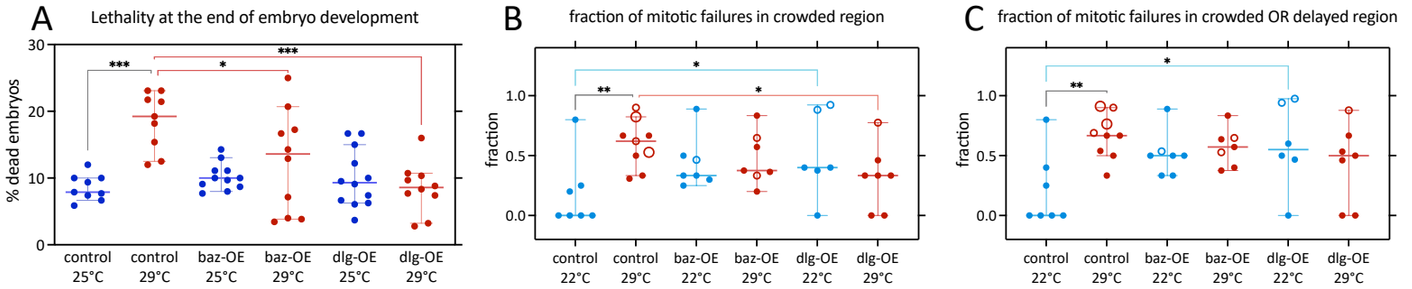

Over-expressing regulators of 'F-actin -microtubule interaction during mitosis'
to rescue embryonic lethality at elevated temperature

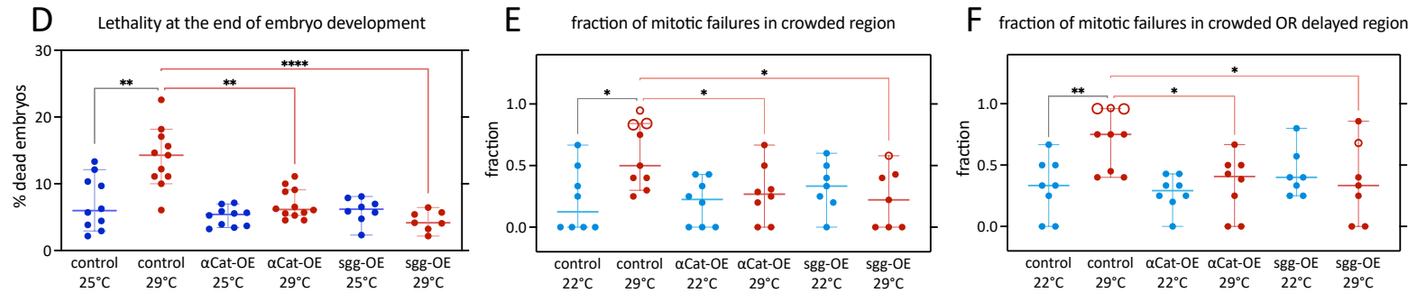

"Natural" candidate genes varying along thermoclines

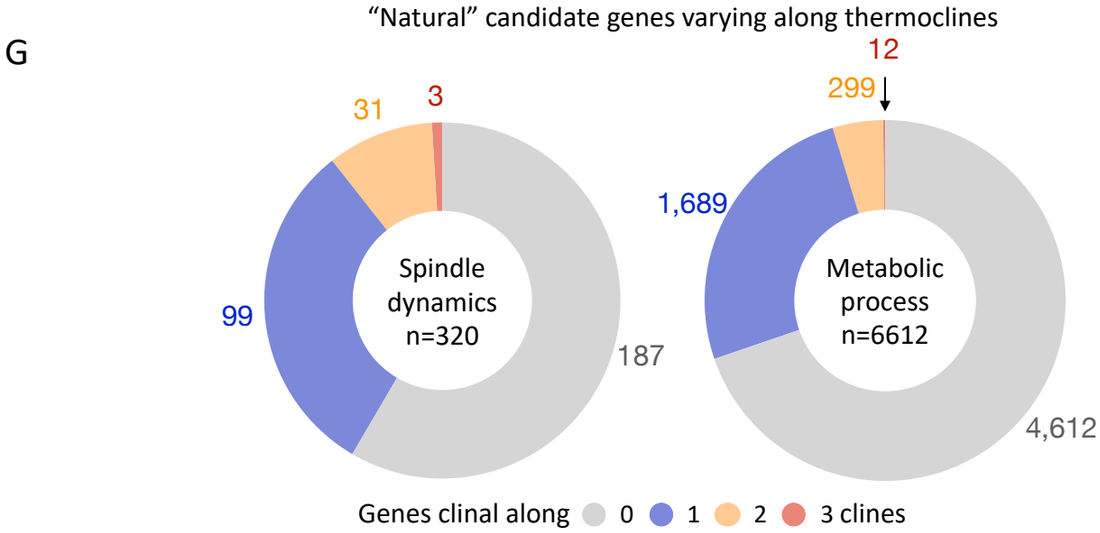

Figure S1

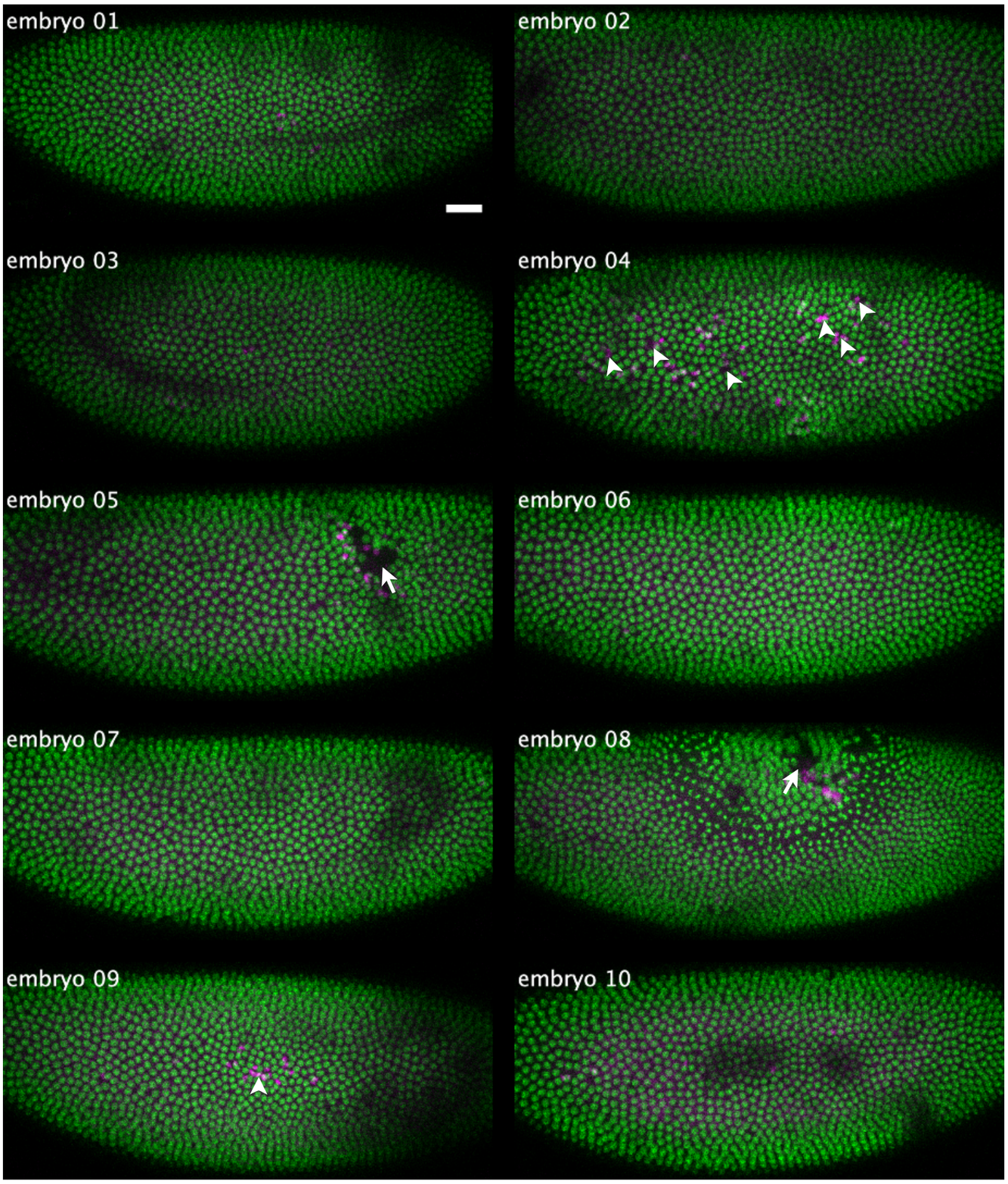
embryo 01
embryo 02
embryo 03
embryo 04
embryo 05
embryo 06
embryo 07
embryo 08
embryo 09
embryo 10

Figure S2

Nuclear loss phenotype due to elevated temperature

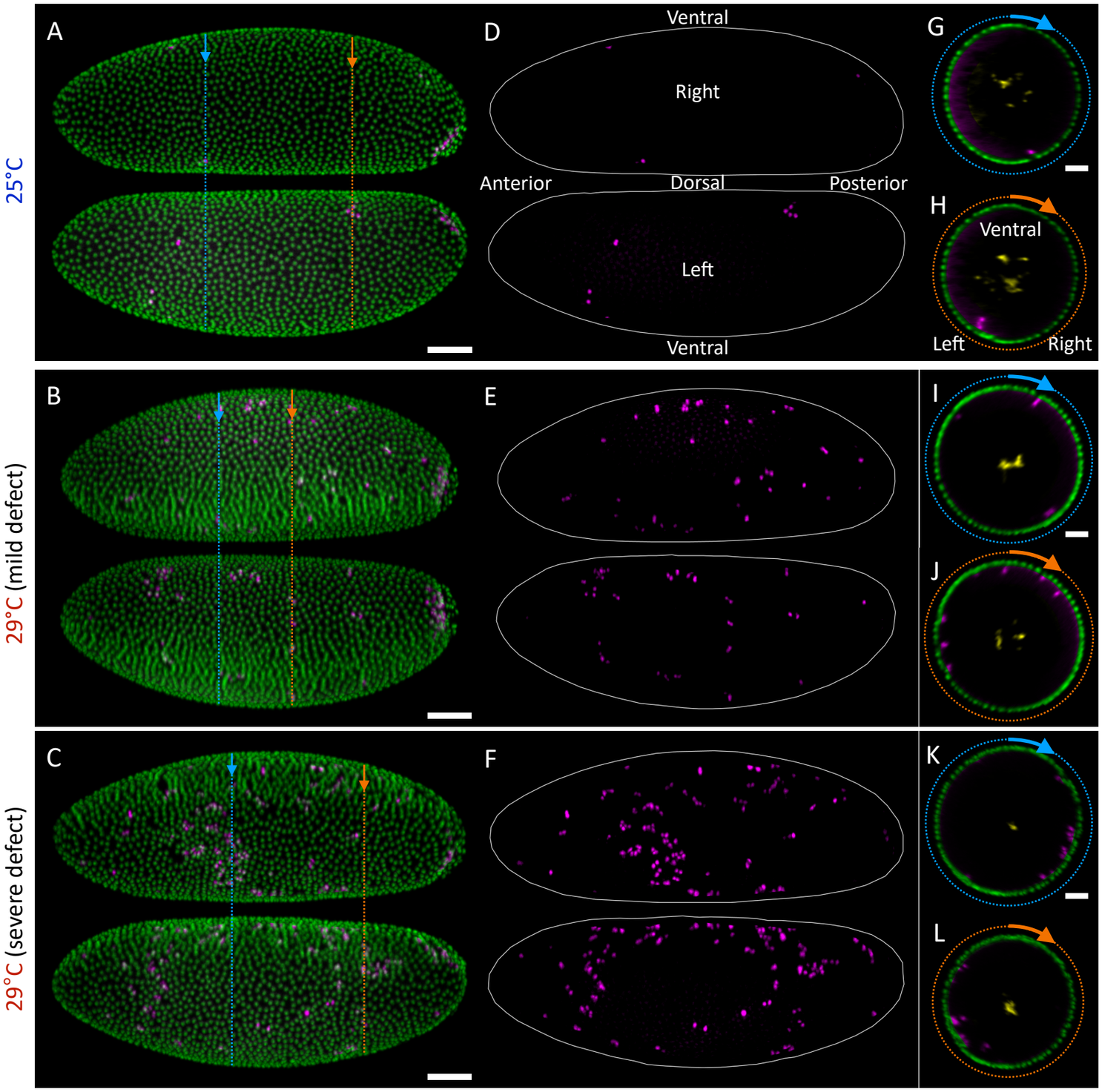

Figure S3

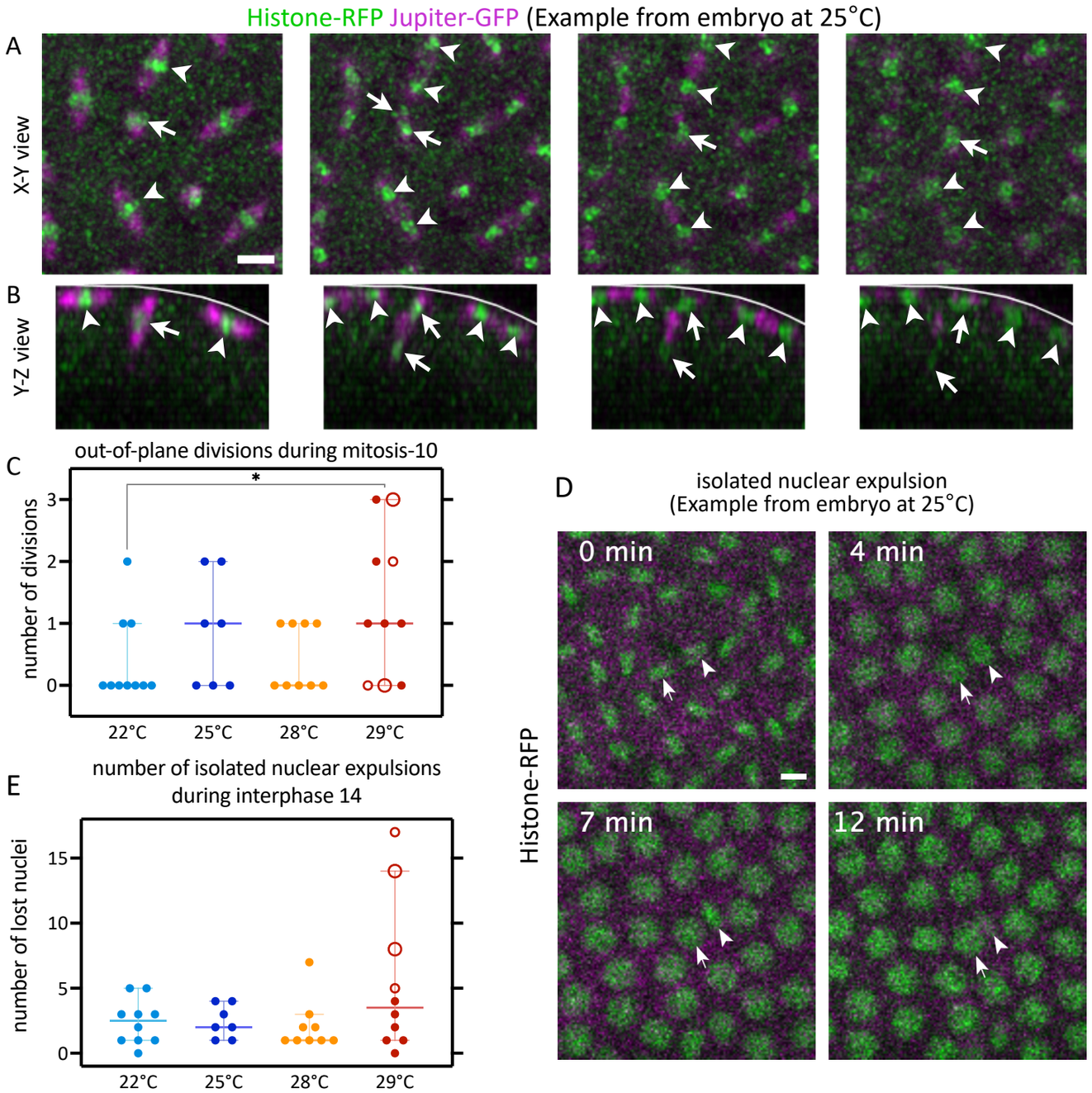
Histone-RFP Jupiter-GFP (Example from embryo at 25°C)
A
X-Y view
B
Y-Z view
C
out-of-plane divisions during mitosis-10
number of divisions
*
22°C
25°C
28°C
29°C
D
isolated nuclear expulsion
(Example from embryo at 25°C)
Histone-RFP
0 min
4 min
7 min
12 min
E
number of isolated nuclear expulsions
during interphase 14
number of lost nuclei
22°C
25°C
28°C
29°C

Figure S4

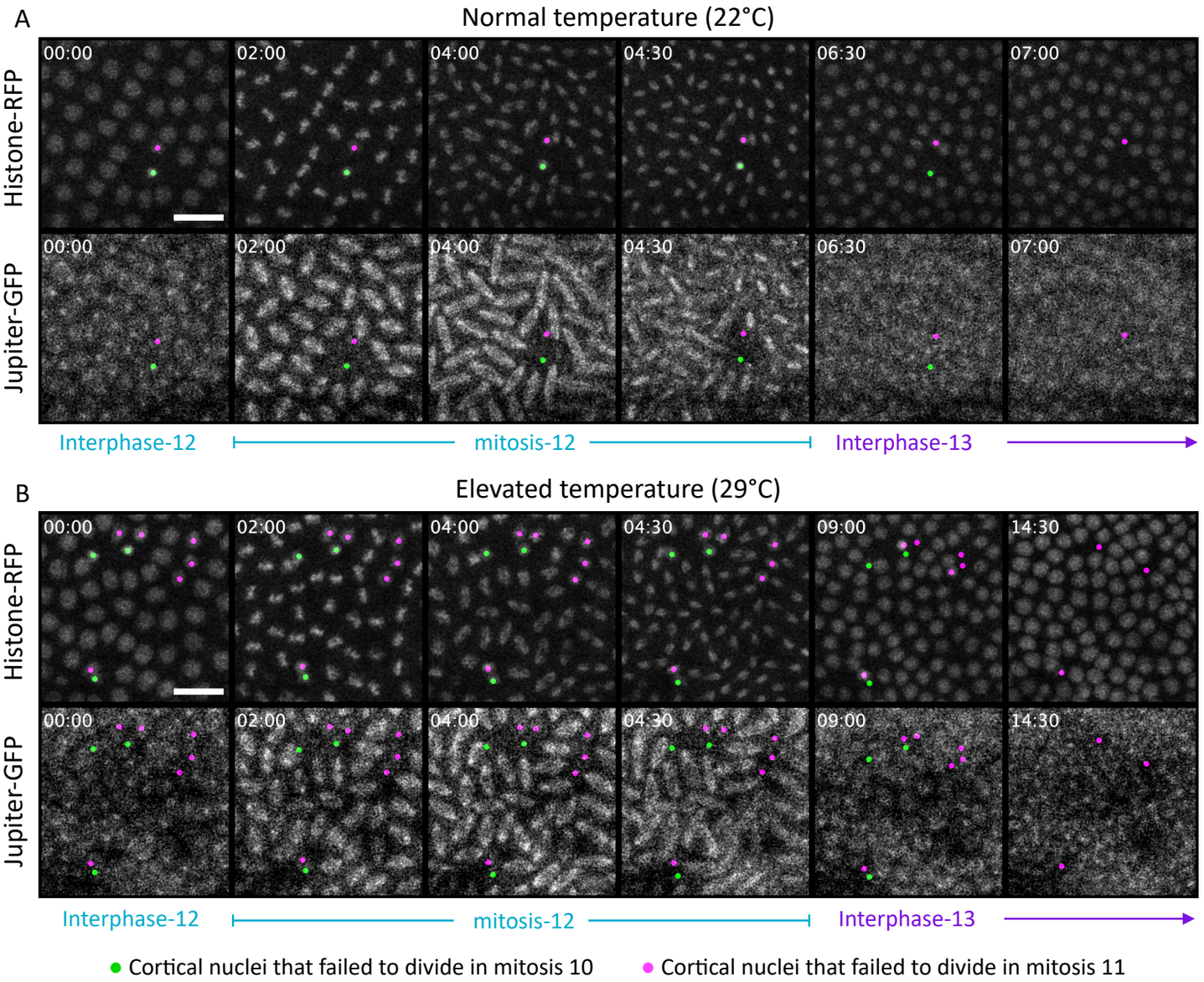
A
Normal temperature (22°C)
Histone-RFP
Jupiter-GFP
00:00
02:00
04:00
04:30
06:30
07:00
Interphase-12
mitosis-12
Interphase-13
B
Elevated temperature (29°C)
Histone-RFP
Jupiter-GFP
00:00
02:00
04:00
04:30
09:00
14:30
Interphase-12
mitosis-12
Interphase-13
Cortical nuclei that failed to divide in mitosis 10
Cortical nuclei that failed to divide in mitosis 11

Figure S5

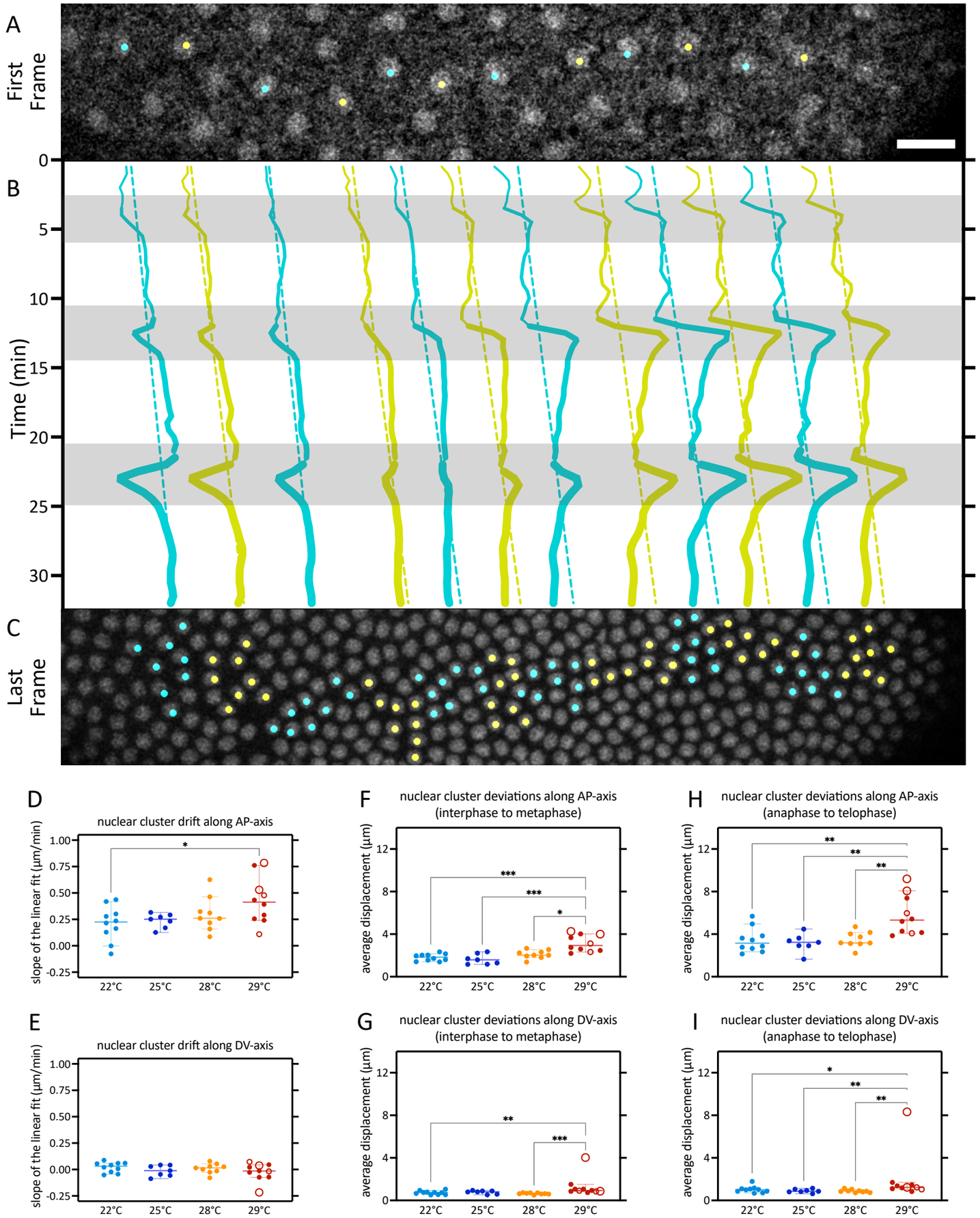
A
First Frame
B
Time (min)
0
5
10
15
20
25
30
C
Last Frame
D
nuclear cluster drift along AP-axis
slope of the linear fit (µm/min)
1.00
0.75
0.50
0.25
0.00
-0.25
*
22°C
25°C
28°C
29°C
E
nuclear cluster drift along DV-axis
slope of the linear fit (µm/min)
F
nuclear cluster deviations along AP-axis
(interphase to metaphase)
average displacement (µm)
12
8
4
0
***
***
*
G
nuclear cluster deviations along DV-axis
(interphase to metaphase)
**
***
H
nuclear cluster deviations along AP-axis
(anaphase to telophase)
**
**
**
I
nuclear cluster deviations along DV-axis
(anaphase to telophase)
*
**
**

Figure S6

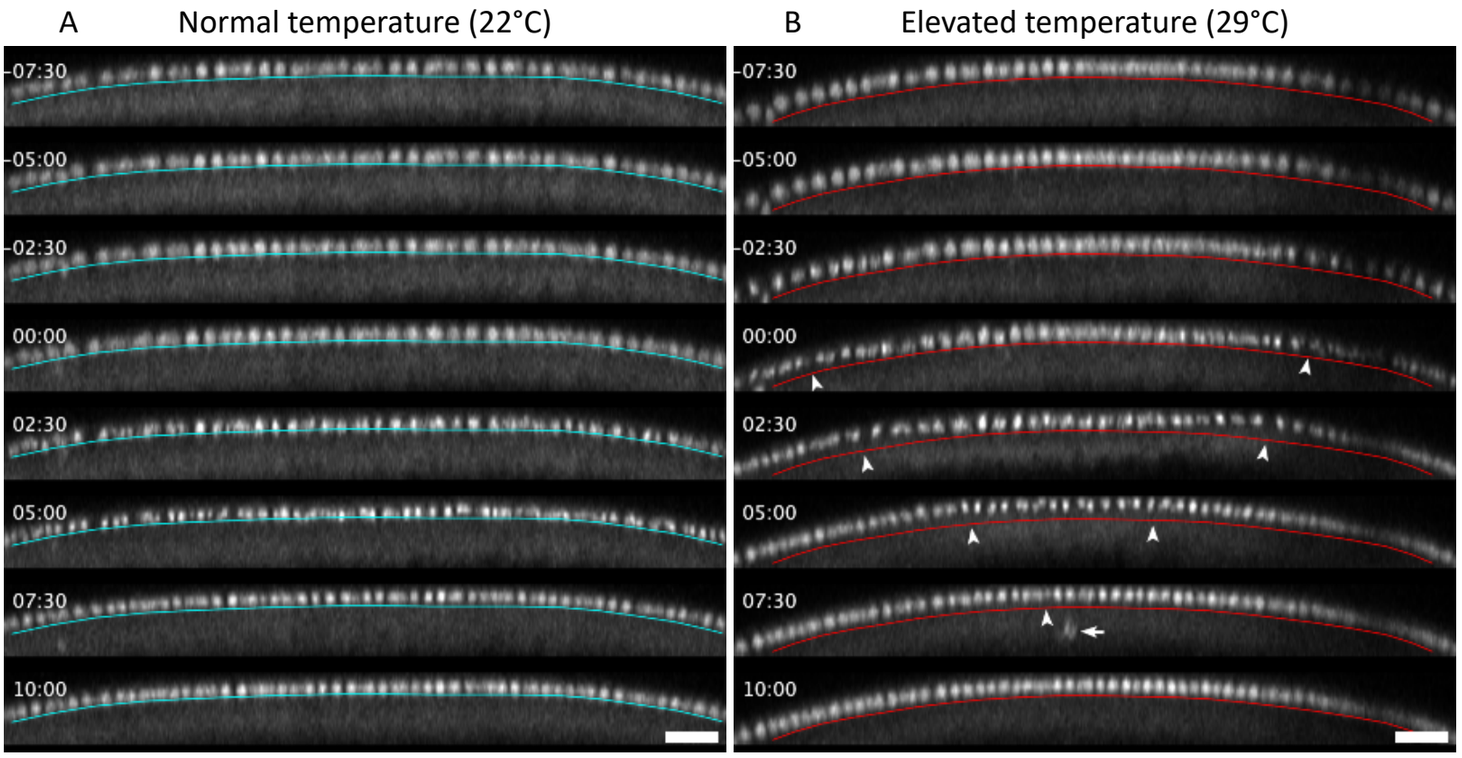
A
Normal temperature (22°C)
B
Elevated temperature (29°C)
07:30
05:00
02:30
00:00
02:30
05:00
07:30
10:00
07:30
05:00
02:30
00:00
02:30
05:00
07:30
10:00

Figure S7

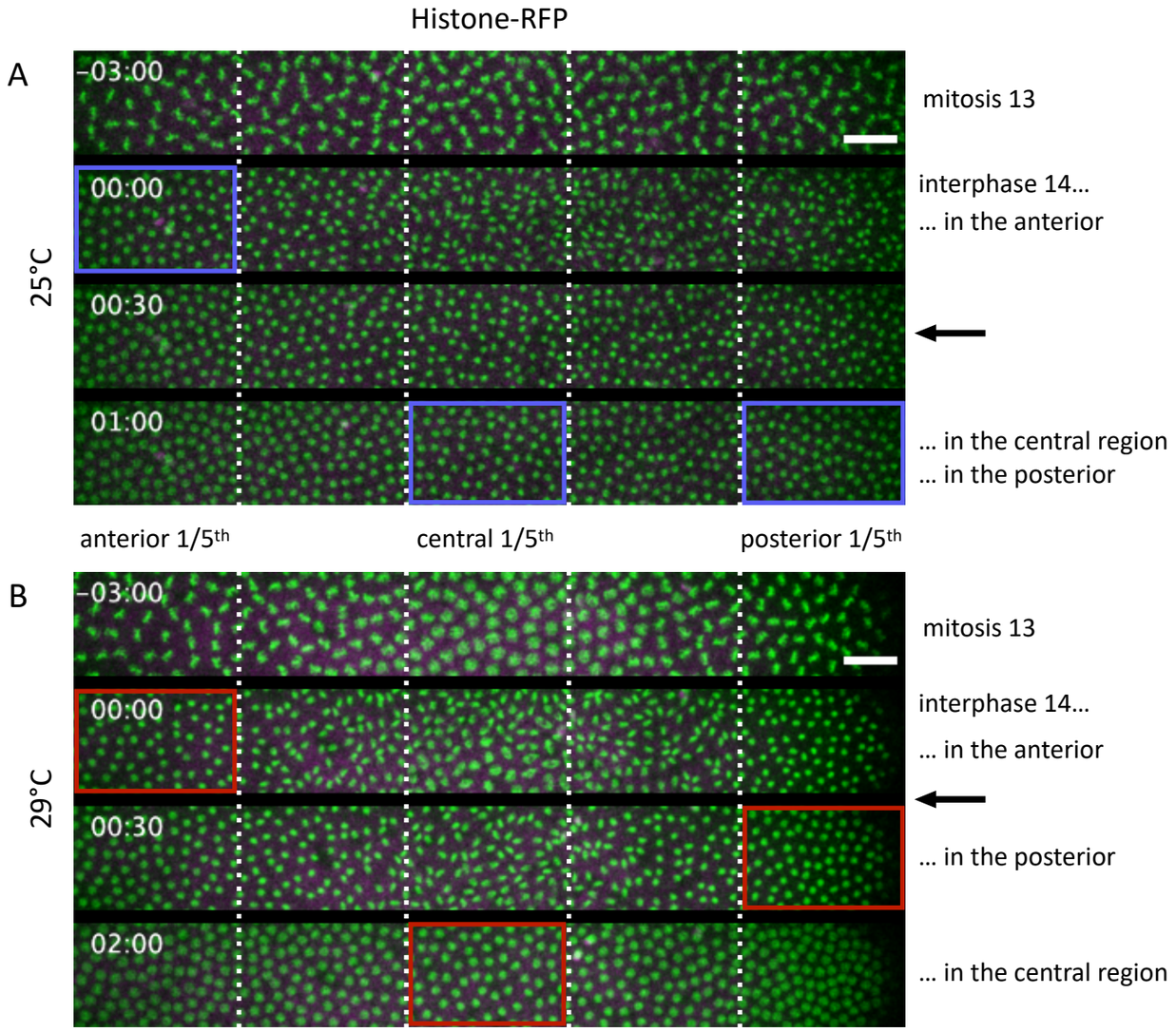
Histone-RFP
A
25°C
-03:00
00:00
00:30
01:00
mitosis 13
interphase 14…
… in the anterior
… in the central region
… in the posterior
anterior 1/5th
central 1/5th
posterior 1/5th
B
29°C
-03:00
00:00
00:30
02:00
mitosis 13
interphase 14…
… in the anterior
… in the posterior
… in the central region

Figure S8

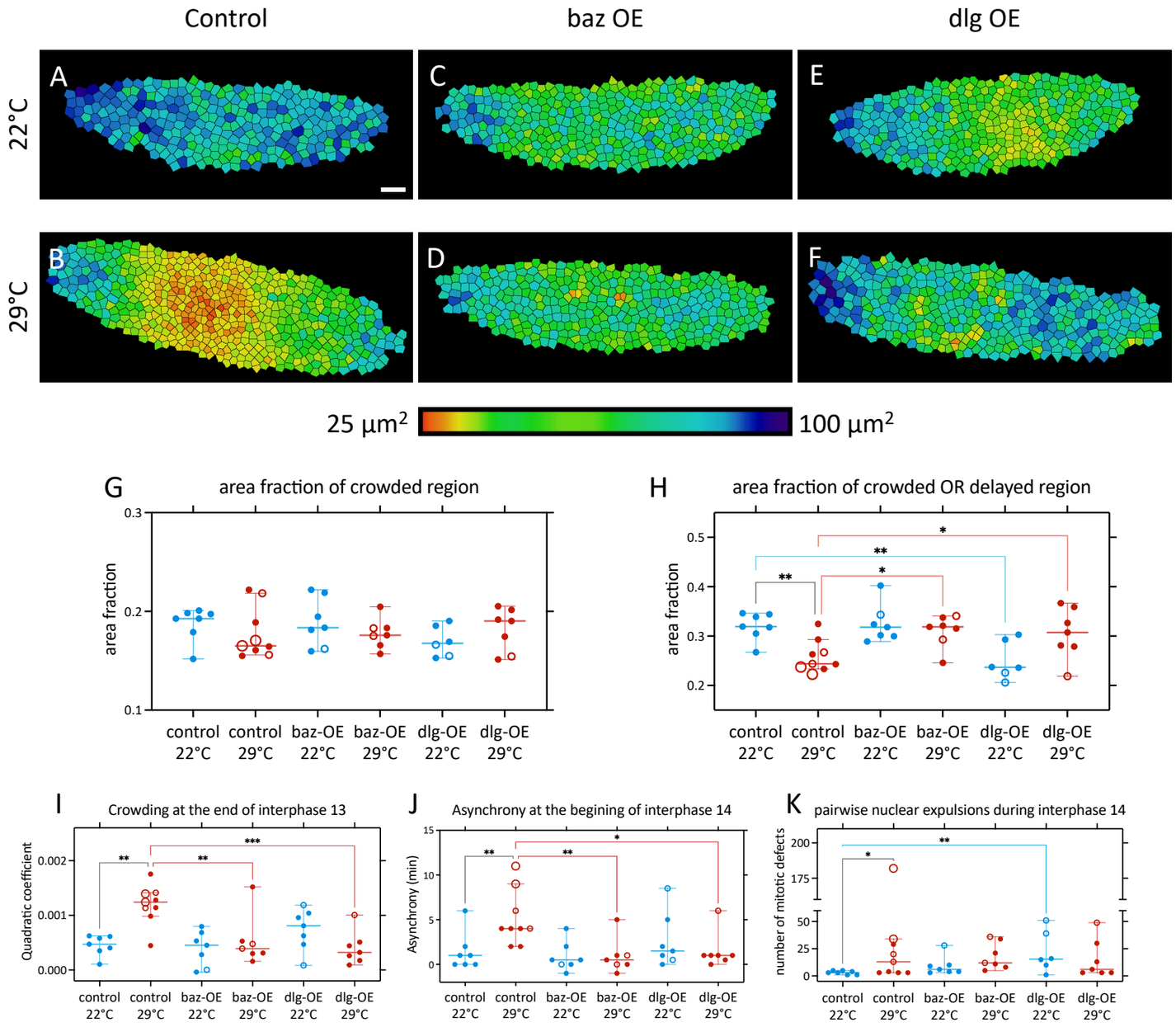
Control
baz OE
dlg OE
22°C
29°C
A
B
C
D
E
F
25 µm²
100 µm²
G
area fraction of crowded region
area fraction
H
area fraction of crowded OR delayed region
I
Crowding at the end of interphase 13
Quadratic coefficient
J
Asynchrony at the begining of interphase 14
Asynchrony (min)
K
pairwise nuclear expulsions during interphase 14
number of mitotic defects
control 22°C
control 29°C
baz-OE 22°C
baz-OE 29°C
dlg-OE 22°C
dlg-OE 29°C

Figure S9

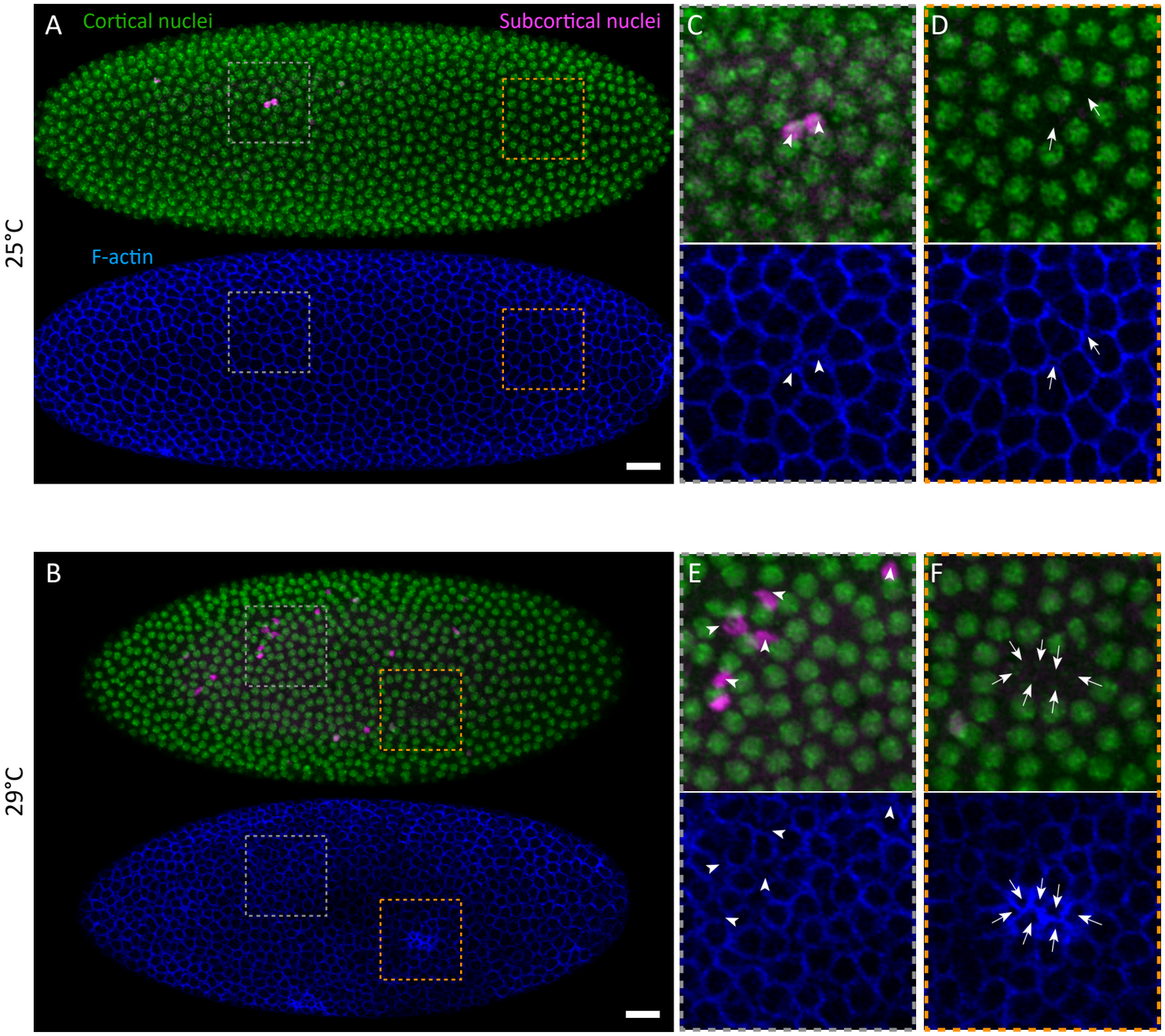

Figure S10

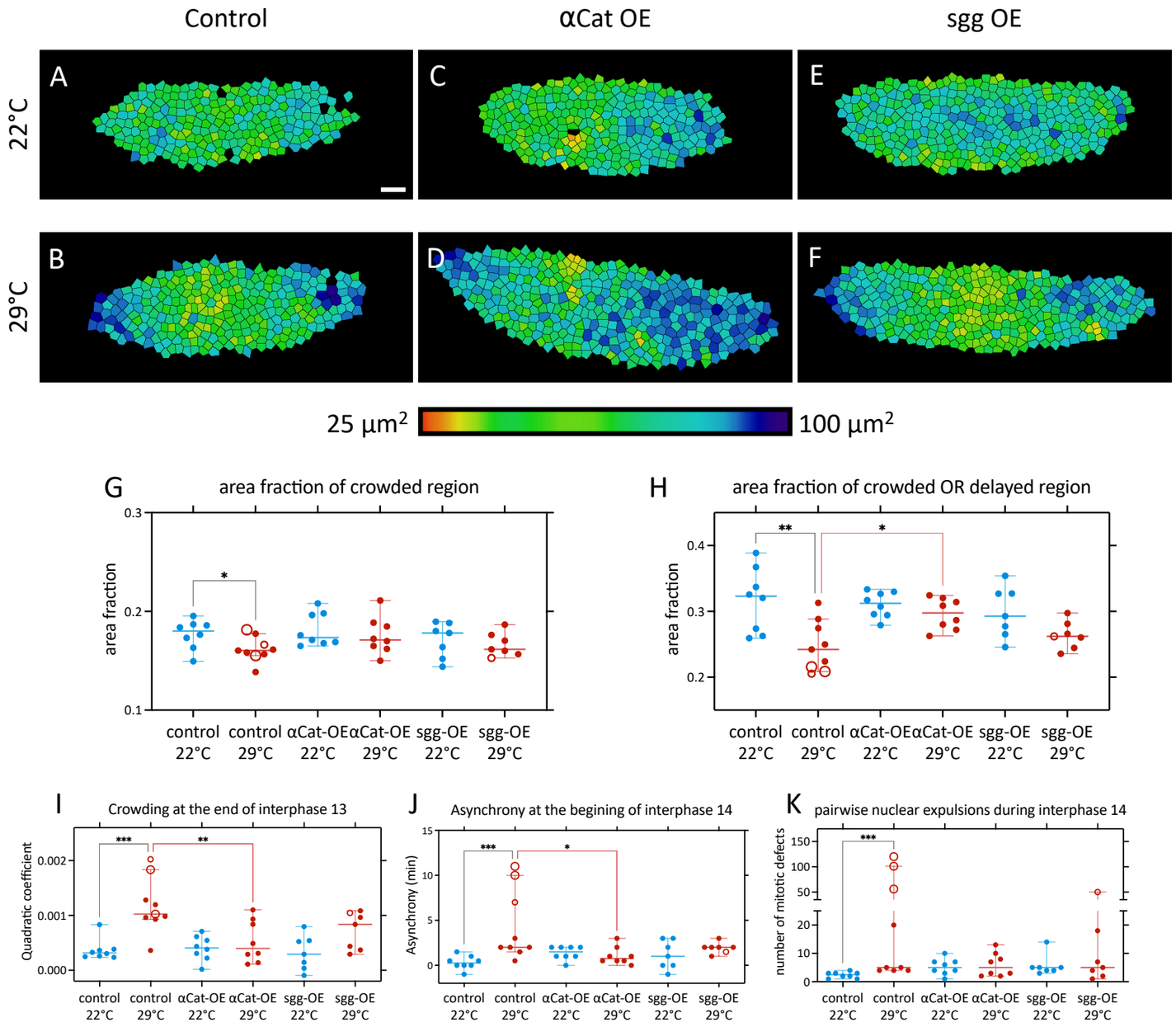
Control
αCat OE
sgg OE
22°C
29°C
A
B
C
D
E
F
25 µm²
100 µm²
G
area fraction of crowded region
area fraction
control 22°C
control 29°C
αCat-OE 22°C
αCat-OE 29°C
sgg-OE 22°C
sgg-OE 29°C
H
area fraction of crowded OR delayed region
I
Crowding at the end of interphase 13
Quadratic coefficient
J
Asynchrony at the begining of interphase 14
Asynchrony (min)
K
pairwise nuclear expulsions during interphase 14
number of mitotic defects

Figure S11

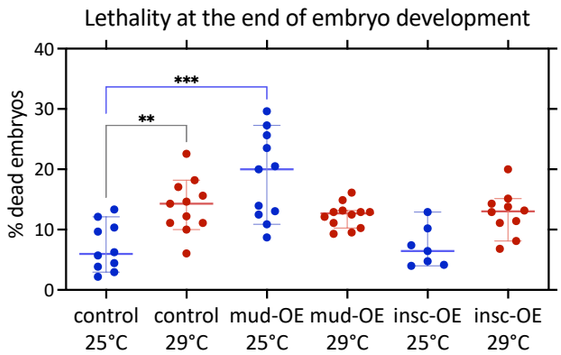
Lethality at the end of embryo development
% dead embryos
40
30
20
10
0
***
**
control 25°C
control 29°C
mud-OE 25°C
mud-OE 29°C
insc-OE 25°C
insc-OE 29°C